Gamma-ray Spectroscopy of $^{7}_{\Lambda}$Li

($^{7}_{\Lambda}$Li ハイパー核の γ 線分光)

谷 田 聖

学位論文

Gamma-ray Spectroscopy of ${}^{7}_{\Lambda}$Li
（${}^{7}_{\Lambda}$Liハイパー核のγ線分光）

平成 11 年 11 月博士（理学）申請

東京大学大学院理学系研究科
物理学専攻

谷田 聖

Abstract

Λ hypernuclei give us invaluable information on the ΛN interaction, especially on the spin-dependent part, via their structure. γ-ray spectroscopy is expected to be a powerful tool to investigate hypernuclear structure utilizing its execellent energy resolution available by using germanium detectors. We have newly constructed a germanium detector system (Hyperball) for the purpose to determine the strength of all the ΛN spin-dependent interactions.

As the first experiment using the Hyperball, we performed a γ-ray spectroscopy experiment of ${}^{7}_{\Lambda}$Li, which is the best hypernuclei to study the ΛN spin-spin interaction. Shrinking effect of a hypernucleus due to the presence of a Λ particle ("glue-like role" of a Λ particle) was also studied in the experiment.

The experiment has been carried out at the KEK-PS K6 beamline using the SKS spectrometer and the Hyperball. ${}^{7}_{\Lambda}$Li hypernuclei were produced by the ^{7}Li(π^+, K^+) reaction, and the γ-rays were measured in coincidence.

We have succeeded in observing two γ-transitions of ${}^{7}_{\Lambda}$Li, namely the $M1(3/2^+ \rightarrow 1/2^+)$ transition and the $E2(5/2^+ \rightarrow 1/2^+)$. This is the first observation of well-identified hypernuclear γ-rays with germanium detectors. The energies of the two transitions were measured to be 691.7 ± 0.6(statistical) ± 1.0(systematic) keV and 2050.4 ± 0.4(statistical) ± 0.7(systematic) keV. The precision of the present results renews the world record of hypernuclear experiments by more than one order of magnitude.

The energy of the $M1$ transition gives direct information on the strength of the ΛN spin-spin interaction. The present result is consistent with the strength estimated from the four-body hypernuclear data. Thus the strength of the ΛN spin-spin interaction is experimentally established.

We also measured the lifetime of the $5/2^+$ state of ${}^{7}_{\Lambda}$Li to be $5.8^{+0.9}_{-0.7}$(statistical)$\pm$ 0.7(systematic) ps from the peak shape of the $E2$ transition. This corresponds to a $B(E2; 5/2^+ \rightarrow 1/2^+)$ value of $3.6 \pm 0.5^{+0.5}_{-0.4}$ e^2fm^4, which gives a clear indication of the shrinkage of ${}^{7}_{\Lambda}$Li and the "glue-like role" of Λ is experimentally verified.

With those results, we have proven the usefulness of γ-ray spectroscopy in studies of hypernuclei. We are planning further experiments on various hypernuclei such as ${}^{9}_{\Lambda}$Be, ${}^{16}_{\Lambda}$O and so on to determine the other spin-dependent interactions and to study further hypernuclear physics.

Contents

List of Figures

List of Tables

Chapter 1

Introduction

1.1 Physics of hypernuclear γ-ray spectroscopy

The ΛN interaction is the first step toward the unified understanding of general baryon-baryon interactions beyond the well-known NN interaction. Since the ΛN interaction contains new information on the baryon-baryon interactions even at the limit of flavor SU(3) symmetry, knowlegde of the ΛN interaction is essential to understand general baryon-baryon interactions. In this point of view, it is an interesting question to be answered whether the ΛN interaction can be represented by meson exchange models in a consistent way with the NN interaction or we have to take into account the quark-gluon degree of freedom. Furthermore, the ΛN interaction is the most fundamental subject in the study of hypernuclei as the NN interaction in the study of ordinary nuclei.

Historically, the NN interaction has been studied by elastic scattering experiments. However, due to the short (263 ps) lifetime of a Λ particle, ΛN scattering experiments are extremely difficult. So far, only a few thousand scattering events have been observed and no data for polarization observables are available. Thus the structures of Λ hypernuclei give us almost unique opportunity to investigate the ΛN interactions, especially spin dependent ones.

In this situation, it has been long recognized that the energy spectra of Λ hypernuclei can provide direct information on the free ΛN interactions. This is because the ΛN interaction is weaker than the NN interaction so that complicating many-body effects are small. This weakness of ΛN interaction comes from the fact that one-pion exchange is forbidden due to isospin conservation. Furthermore, the fact that the Λ particle in a Λ hypernucleus is free from Pauli blocking,

at least in the baryon level, makes ambiguities of the hypernuclear sturucture small.

The ΛN (effective) interaction includes spin-independent central force, spin-spin force, spin-orbit forces and tensor force, and is usually expressed as;

$$V = V_c(r) + V_\sigma(r)\vec{\sigma}_\Lambda \cdot \vec{\sigma}_N + V_\Lambda(r)\vec{L} \cdot \vec{\sigma}_\Lambda + V_N(r)\vec{L} \cdot \vec{\sigma}_N + V_T(r)\left\{\frac{3(\vec{\sigma}_\Lambda \cdot \vec{r})(\vec{\sigma}_N \cdot \vec{r})}{r^2} - \vec{\sigma}_\Lambda \cdot \vec{\sigma}_N\right\},$$

where $\vec{L}$ and $\vec{r}$ are the ΛN relative orbital angular momentum and position, respectively, and σ_x denotes the spin of a particle x. Among those interactions, the strength of the spin-independent central force $[V_c(r)]$ is relatively well known from the binding energies of Λ hypernuclei over a wide range of mass number. Binding energies of Λ hypernuclei can be well reproduced by a simple Woods-Saxon type single particle potential of which depth is 30 MeV [1]. On the other hand, the spin-dependent terms are hardly known.

Spin-dependent interactions can be studied from the structure of hypernuclei in the following way. Suppose there is a normal nucleus with spin $j(\neq 0)$, and a Λ particle is added to it in the 0s state. Since a Λ has spin 1/2, the state splits into two states of which spins are $j + 1/2$ and $j - 1/2$ (See Figure 1.1). The spatial wave functions of the two states are the same given the ΛN interaction is weak enough. Therefore, the energy splitting of the two states is determined only by the ΛN spin-dependent interactions. In γ-ray spectroscopy, the energy splitting can be obtained by measuring the energies of either the γ_1 or γ_2 and γ_3 in the figure.

For p-shell hypernuclei, the integral of the spin-dependent terms over the shell model wavefunctions are often expressed as Δ, S_Λ, S_N and T, according to Ref. [2, 3]. Δ is defined as

$$\Delta = \int \phi^*_{\Lambda N}(\vec{r}) V_\sigma(r) \phi_{\Lambda N}(\vec{r}) d\vec{r},$$

where $\phi_{\Lambda N}(\vec{r})$ is the ΛN relative spatial wavefunction for $p_N s_\Lambda$ state. Similarily, the others are defined from $V_\Lambda(r)$, $V_N(r)$ and $V_T(r)$. They can be treated as parameters which are to be determined phenomenologically by fitting the data of p-shell hypernuclear level energies. It is noted that those parameters can be taken to be constant throughout the p-shell hypernuclei in a good approximaion [3]. Table 1.1 shows the values of those parameters in various theories.

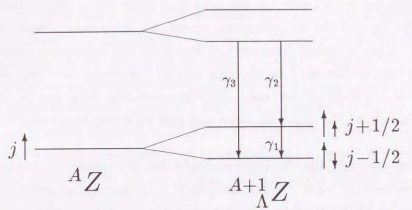

Figure 1.1: *Level splitting of hypernuclei caused by spin-dependent interactions and γ-rays.*

Table 1.1: *Theoretical values of $p_N s_\Lambda$ interaction parameters. All the values are written in the unit of MeV. The first two parameter sets are taken from phenomenological study of Millener* et al. *[3] and Fetisov* et al. *[4]. The other parameter sets are calculated from meson exchange potential models of the Nijmegen group (ND, NF, NSC89 and NSC97f) and the Jülich group (JA and JB) by Millener [5].*

	Δ	S_Λ	S_N	T
Millener [3]	0.50	−0.04	−0.08	0.04
Fetisov [4]	0.30	−0.02	−0.10	0.02
ND [6]	−0.048	−0.131	−0.264	0.018
NF [7]	0.072	−0.175	−0.266	0.033
NSC89 [8]	1.590	−0.173	−0.292	0.036
NSC97f [9]	0.754	−0.140	−0.257	0.054
JA [10]	−0.478	−0.124		
JB [10]	−1.596	−0.129		

1.1.1 Spin-spin interaction

As we can see from Table 1.1, the spin-spin force varies largely model by model. Even the sign of the Δ parameter cannot be determined from those potential models. This is mainly because the available ΛN scattering cross section data contain information only on the sum of the S-wave interactions, but not on the indivisual $^1S_0$ and $^3S_1$ channels. Thus hypernuclear data can provide unique information about the spin-spin force and give stringent constraint to the potential models.

Experimentally, the observation of spin-flip $M1$ transitions between the ground state doublets ($1^+ \to 0^+$) of $^4_\Lambda$H and $^4_\Lambda$He [11, 12] gave information of the spin-spin interaction. Millener *et al.* [3] estimated the strength of the spin-spin force by the measured energy splittings of about 1.1 MeV and obtained $\Delta \sim 0.5$ MeV. The binding energies of the ground states of $^7_\Lambda$Li and $^7_\Lambda$Be gave a similar value of $\Delta \sim 0.50 \pm 0.11$ MeV in his analysis, assuming the charge independence of the ΛN interaction.

This estimation, however, could not settle the value of the Δ parameter, because it failed to reproduce a null result of the $^{10}_\Lambda$B experiment by Chrien *et al.* [13]. Millener predicted 170 keV for the splitting of the ground state doublet ($1^-, 2^-$, the 1^- state was the ground state in his calculation), but the spin-flip $M1(2^- \to 1^-)$ transition was not observed in the experiment between 100 keV and 900 keV. This suggests that the splitting is smaller than 100 keV or the 2^- state is the ground state. Fetisov *et al.* [4] proposed another value of $\Delta = 0.3$ MeV to explain the result.

Furthermore, Gibson *et al.* [14] pointed out that ΛN-ΣN coupling effect can affect the splitting of the ground state doublet of four body hypernuclei. According to their estimation, such effect can explain the observed splitting even if we take the spin-spin force is zero. They concluded that the measured energy spilitting in the four body hypernuclei "is *not* a measure of the ΛN spin-spin interaction". Thus we need more data to determine the strength of the spin-spin interaction, especially, on hypernuclear states for which the ΛN-ΣN coupling effect is expected to be small.

1.1.2 Spin-orbit interactions

From the past experiments it is known that the spin-orbit force which couples to the spin of Λ ($V_\Lambda(r)$, S_Λ) is small compared to the nucleon case. For example,

the experiment on $^9_\Lambda$Be by May *et al.* [15] suggests a very small value including zero for S_Λ ($|S_\Lambda| < 0.04$ MeV [3]). On the other hand, re-analysis of emulsion experiments on $^{16}_\Lambda$O [16] and recent experiments of $^{89}_\Lambda$Y [17, 18] might give larger spin-orbit interactions, as large as $1/5 \sim 1/3$ of the nucleon case for the Λ single particle potential (corresponding to an S_Λ value of $-0.2 \sim -0.3$ MeV).

Most of the meson exchange models predict relatively large values, as shown in Table 1.1, which are almost consistent with the results of the latter two experiments. On the other hand, it is pointed out that since spin-orbit force has short-range nature, quark-gluon degree of freedom should be explicitly taken into account. In calculations based on this notion, $V_\Lambda(r)$ is much weaker [19, 20, 21], being consistent with the $^9_\Lambda$Be experiment.

As for the other spin-orbit force ($V_N(r)$, S_N), we cannot extract strength information from the energy splitting of hypernuclear doublets since it does not couple to the spin of Λ. Still, it can be obtained by measuring the change of level energies of core nuclei. Recent experimetal results on core excitation states of several hypernuclei such as $^{13}_\Lambda$C [22] suggests a relatively large value of $S_N \sim -0.5$ MeV [26] in comparison to S_Λ.

1.1.3 Tensor interaction

As for the tensor interaction, there are no experimental data at all which give direct information. Naively, the tensor force is thought to be small because the one pion exchange, which is the main source of the NN tensor force, is forbidden.

1.2 Merit of γ-ray spectroscopy

The largest merit of γ-ray spectroscopy is its excellent energy resolution. In hypernuclear experiments, the best energy resolution so far achieved with magnetic spectrometers was about 2 MeV (FWHM) with SKS spectrometer [23]. On the other hand, by γ-ray spectroscopy, an energy resolution of $\sim$ 100 keV can be easily achieved with NaI counters, and with germanium detectors, it can be improved down to 2 keV, which is by three orders of magnitude better than that of a magnetic spectrometers. Since the energy splitting due to ΛN spin dependent forces are expected to be less than 1 MeV in most cases, and often less than 100 keV, this excellent resolution is essential for studies of hypernuclei and ΛN interaction.

Another merit is that using γ-ray spectroscopy, we can also study those states which cannot be directly populated. For example, suppose the case that the $j+1/2$ state in Figure 1.1 can not be populated via direct reactions. It is usually the case for experiments with the (π^+, K^+) and (K^-, π^-) reactions because of their spin non-flip nature of Λ production (see Appendix A). Still, the state can be studied by γ-ray spectroscopy, because γ-ray cascade process from upper states (γ_2 in the figure, for example) can also populate the state.

1.3 Past γ-ray spectroscopy experiments of hypernuclei

In spite of the merits of γ-ray spectroscopy explained above, there have been few experiments of the γ-ray spectroscopy of hypernuclei. Only five γ-transitions have been identified and established so far, all of which were observed using NaI counters.

At CERN, γ-rays from ${}^{4}_{\Lambda}$H and ${}^{4}_{\Lambda}$He were observed in coincidence with their weak decays [11, 12]. They are spin-flip M1 transitions between the ground state doublets ($1^+ \to 0^+$), and the energies of the γ-rays (~ 1.1 MeV) provide unique data for the ΛN spin-spin interaction.

γ-rays from ${}^{7}_{\Lambda}$Li and ${}^{9}_{\Lambda}$Be were observed by May *et al.* [15] at BNL. They created these hypernuclei by the (K^-, π^-) reaction and measured γ-rays in coincidence. Figure 1.2 shows the γ-ray spectra for the ${}^{7}_{\Lambda}$Li case. The 2.034 ± 0.023 MeV γ-ray was assigned to the $E2(5/2^+ \to 1/2^+)$ transition, which is essentially the same as the ^{6}Li core transition, $3^+ \to 1^+$. As for ${}^{9}_{\Lambda}$Be, they observed only one γ-ray peak at 3.079 ± 0.040 MeV, while two transitions ($5/2^+ \to 1/2^+$ and $3/2^+ \to 1/2^+$) are expected. Their conclusion was that the energies of those transitions are too close (< 100 keV in 95% confidence level) to see separated peaks.

Another experiment at BNL succeeded in observing a γ-ray from ${}^{13}_{\Lambda}$C [24]. The experimental method was the same as the last experiment, and the 11 MeV γ-ray emitted by the $E1$ transition $1/2^-(\Lambda_{p_{1/2}} \otimes {}^{12}\mathrm{C}_{\mathrm{g.s.}}) \to 1/2^+(\Lambda_{s_{1/2}} \otimes {}^{12}\mathrm{C}_{\mathrm{g.s.}})$ was observed.

There has been only one experiment which tried to measure hypernuclear γ-rays with germanium detectors [13]. They did not observe the γ-ray of the spin-flip $M1$ transition between the ground state doublet $(2^-, 1^-)$ of ${}^{10}_{\Lambda}$B.

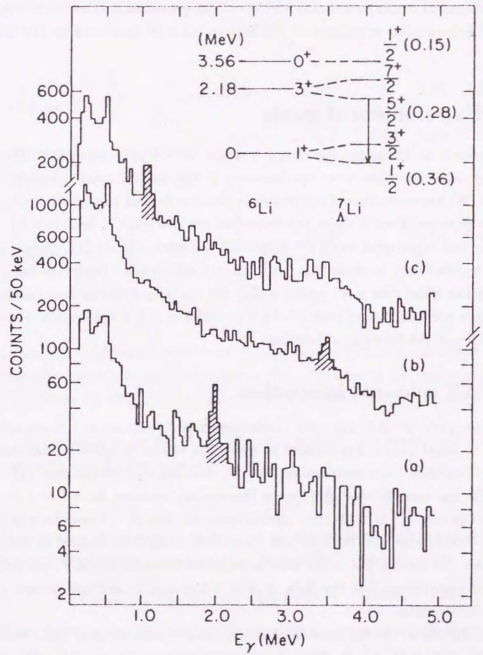

Figure 1.2: *γ-ray spectrum of ${}^{7}_{\Lambda}$Li measured in the (K^-, π^-) reaction at BNL using NaI counters [15]. When the bound state region is gated [(a)], they observed a peak at 2.03 MeV which is attributed to the E2 transition of $5/2^+ \to 1/2^+$. However, they could not measure the rate of the transition, nor observe the $M1(3/2^+ \to 1/2^+)$ transition.*

The scarceness of the hypernuclear γ-ray spectroscopy experiments with germanium detectors is due to difficulties in operating germanium detectors in conditions of hypernuclear experiments. See Section 2.3.1 for details about the difficulties.

1.4 Experimental goals

Our purpose is to determine the strength of all the ΛN spin dependent interactions by high-resolution γ-ray spectroscopy of hypernuclei using germanium detectors. We have constructed a germanium detector system named "Hyperball" for this purpose. Details about the Hyperball are described in Section 2.3.1.

As the first experiment using the Hyperball, we have selected ${}^{7}_{\Lambda}$Li, since it is the best hypernucleus to study the ΛN spin-spin interaction. Furthermore, we can study the effect that a Λ particle makes the size of a hypernucleus smaller than its core nucleus ("glue-like role" of a Λ particle) in ${}^{7}_{\Lambda}$Li. I will describe those two purposes in the follwoing subsections.

1.4.1 ΛN spin-spin interaction

In order to study the ΛN spin-spin interaction from hypernuclear structure, it is better to select proper hypernuclei in which the effects of other interactions are small. In p-shell hypernuclei except for ${}^{7}_{\Lambda}$Li, the spin-orbit interaction $[V_{\Lambda}(r), S_{\Lambda}]$ usually has considerable effect since the valence nucleons have $l = 1$ (see below for the case of ${}^{7}_{\Lambda}$Li). All the s-shell hypernuclei but $A = 4$ ones have only one or no bound state, so the spin-spin interaction cannot be studied in those hypernuclei. Therefore, ${}^{7}_{\Lambda}$Li is the best hypernuclei to study the ΛN spin-spin interaction considering that the data of $A = 4$ hypernuclei are not enough to establish its strength.

Figure 1.3 shows the expected level scheme and γ transitions of ${}^{7}_{\Lambda}$Li. Since the ground state (1^+) of core ^{6}Li nucleus has almost pure ${}^{3}S_1$ configuration in which the orbital angular momentum of valence proton and neutron cancels each other, the energy spacing of the ground state doublet $(3/2^+, 1/2^+)$ is determined only by the ΛN spin-spin interaction. Thus we can extract the information of the spin-spin interaction by observing the γ-ray emitted by the spin-flip $M1(3/2^+ \rightarrow 1/2^+)$ transition through its energy. This transition was not observed in the old experiment with NaI counters due to the limited energy resolution.

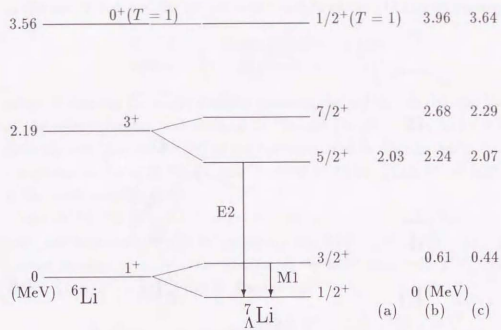

Figure 1.3: *Expected level scheme of ${}^{7}_{\Lambda}$Li with theoretically calculated or experimentally measured excitation energies. (a): Experiment by* May et al. *[15]. (b): Calculation by Millener* et al. *[3]. (c): Calculation by Fetisov* et al. *[4].*

In the simplest model of the LS coupling limit, the energy spilitting can be expressed only by the Δ parameter as;

$$E(3/2^+) - E(1/2^+) = \frac{3}{2}\Delta. \tag{1.1}$$

More precise calculation of Millener *et al.* [3], based on shell-model with Cohen-Kurath [25] effective interactions for the core ^{6}Li nucleus gives

$$E(3/2^+) - E(1/2^+) = 1.35\Delta + 0.15S_{\Lambda} - 0.06S_N - 1.30T. \tag{1.2}$$

Recently, Millener [26] updated the calculation with another effective interaction for the ^{6}Li core which reproduces the structure of the ^{6}Li nucleus better than Cohen-Kurath interactions. It gives

$$E(3/2^+) - E(1/2^+) = 1.444\Delta + 0.054S_{\Lambda} + 0.016S_N - 0.271T \tag{1.3}$$

for the energy splitting.

As for the ΛN-ΣN coupling effect, Akaishi [27] calculated the effect for various s-shell and p-shell hypernuclei and pointed out that the effect is small and thus

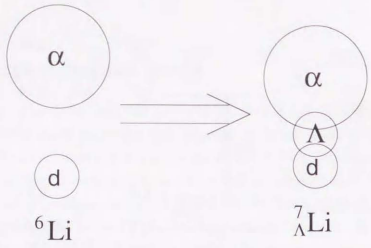

Figure 1.4: *"Glue-like role" of a Λ particle and shrinkage of* $^{7}_{\Lambda}$*Li.*

the strength of the spin-spin force can be obtained by measuring the energy splitting in $^{7}_{\Lambda}$Li.

1.4.2 Verification of the "glue-like role" of Λ

"Glue-like role" of a Λ particle is first pointed out by Motoba *et al.* [28] in cases of hypernuclei which have loosely bound core, such as $^{7}_{\Lambda}$Li. Since a Λ particle in a nucleus is not affected by Pauli blocking, the Λ can locate at the center of the nucleus. Then the Λ attracts nucleons around it, thus makes the hypernucleus shrink (see Figure 1.4 for the case of $^{7}_{\Lambda}$Li). According to a cluster model calculation by Hiyama *et al.* [29], the size of $^{7}_{\Lambda}$Li is predicted to be smaller than ^{6}Li by 25%.

To verify this effect in $^{7}_{\Lambda}$Li, we used the reduced transition rate of the $E2(5/2^+ \rightarrow 1/2^+)$ transition, which is basically the same as the $E2(3^+ \rightarrow 1^+)$ transition of the ^{6}Li core nucleus. The energy of this transition was determined to be 2.034 ± 0.023 MeV in the old experiment with NaI counters, but the transition rate was not measured.

Since the reduced transition rate of an $E2$ transition [$B(E2)$] is proportional

to the fourth order of the nuclear size, the size of the $^{7}_{\Lambda}$Li can be represented as;

$$\frac{R(^{7}_{\Lambda}\mathrm{Li})}{R(^{6}\mathrm{Li})} = \left(\frac{9}{7}\frac{B(E2;\, ^{7}_{\Lambda}\mathrm{Li}\ 5/2^+ \rightarrow 1/2^+)}{B(E2;\, ^{6}\mathrm{Li}\ 3^+ \rightarrow 1^+)}\right)^{1/4}, \tag{1.4}$$

where R denotes the mean distance between the $\alpha(^{5}_{\Lambda}\mathrm{He})$ cluster and the center of the valence proton and neutron in ^{6}Li and $^{7}_{\Lambda}$Li [30]. The factor 9/7 comes from the fact that the $B(E2)$ of the core transition is distributed to the two $E2$ transitions in $^{7}_{\Lambda}$Li as $B(E2;\, ^{7}_{\Lambda}\mathrm{Li}\ 5/2^+ \rightarrow 1/2^+) : B(E2;\, ^{7}_{\Lambda}\mathrm{Li}\ 5/2^+ \rightarrow 3/2^+) = 7 : 2$ in the weak coupling limit.

As $B(E2;\, ^{6}\mathrm{Li}\ 3^+ \rightarrow 1^+)$ is known [31] to be $10.9 \pm 0.9\ e^2\mathrm{fm}^4$, we can extract the hypernuclear size information from $B(E2;\, ^{7}_{\Lambda}\mathrm{Li}\ 5/2^+ \rightarrow 1/2^+)$. What we can measure directly is the lifetime of the $5/2^+$ state [$\tau(5/2^+)$], from which $B(E2;\, ^{7}_{\Lambda}\mathrm{Li}\ 5/2^+ \rightarrow 1/2^+)$ can be derived by:

$$B(E2;\, 5/2^+ \rightarrow 1/2^+) = \frac{BR(5/2^+ \rightarrow 1/2^+)}{\tau(5/2^+)}\frac{75\hbar}{4\pi}\left(\frac{\hbar c}{E}\right)^5, \tag{1.5}$$

where $BR(5/2^+ \rightarrow 1/2^+)$ is the branching ratio of the $E2(5/2^+ \rightarrow 1/2^+)$ transition and E is the energy of the transition. In the present experiment, $\tau(5/2^+)$ was measured by using the Doppler shift attenuation method (see Section 5.3.2).

Chapter 2

Experimental Setup

2.1 Overview of the experiment

The experiment was performed at the KEK-PS K6 beamline with the Superconducting Kaon Spectrometer (SKS) [23] and the Hyperball. Figure 2.1 shows the schematic view of the whole experimental setup.

We used the ^{7}Li(π^+, K^+) reaction to produce $^{7}_{\Lambda}$Li hypernuclei. Beam pions and outgoing kaons were identified and momentum analyzed by the beamline spectrometer and SKS, respectively. With those information obtained by spectrometers, production of the bound states of $^{7}_{\Lambda}$Li can be tagged. γ-rays were measured in coincidence with the (π^+, K^+) reaction by the Hyperball installed in the target region.

In the following sections, details of these experimental components are described. Trigger system and data acquisition system are also described in this chapter.

2.2 Production and tagging of $^{7}_{\Lambda}$Li

2.2.1 KEK-PS K6 beamline

The K6 beamline is located at the North Counter Hall of the KEK-PS. Protons accelerated to 12 GeV by KEK-PS bombarded the production target made of 60 mm long platinum. Produced particles were transported through the magnets from D1 to Q10 to the experimental target. Central momentum of the beam was selected to be 1.05 GeV/c, because the cross section of the elementary process,

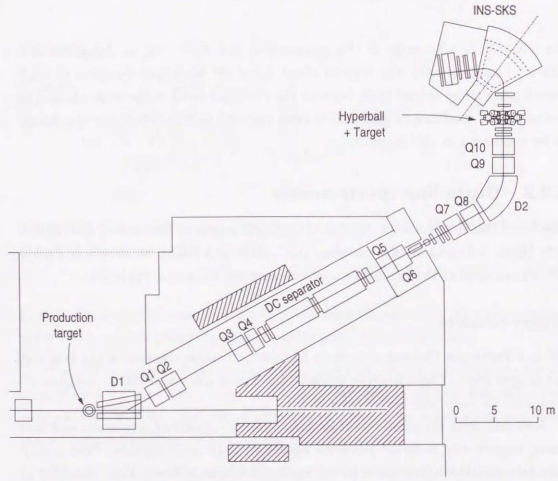

Figure 2.1: *Schematic layout of the whole experimental setup.*

Table 2.1: *Parameters of the beam line spectrometer.*

Momentum resolution	0.1% (FWHM)
Momentum bite	±3%
Maximum central momentum	1.2 GeV/c
Bending angle	60°

$n(\pi^+, K^+)\Lambda$, is maximum at this momentum (see Ref. [32] or Appendix A). The π^+ beam intensity was kept to about 1.8×10^6 for a spill duration of ~0.7 second per a three second cycle because the expected yield of the γ-rays from ${}^{7}_{\Lambda}$Li including the deadtime of germanium detectors and analysis efficiency was found to be maximum at this intensity.

2.2.2 Beam line spectrometer

The beam line spectrometer consists of QQDQQ magnets, four sets of drift chambers (BDC 1-4) and trigger counters (GC, BH1 and BH2), as shown in Figure 2.2. Parameters of the beam line spectrometer are shown in Table 2.1.

Trigger counters

GC is a Freon gas Cherenkov counter to reject e^+ contamination in the beam at the trigger level. The refractive index of the Freon gas was 1.00245, and the e^+ rejection efficiency was better than 99.9%.

BH1 and BH2 are plastic scintillation counters segmented into seven and four parts, respectively, to avoid problems caused by high counting rate. Proton contamination in the beam was rejected by time-of-flight between BH1 and BH2 at the trigger level. BH2 also served as a time zero counter of the whole experiment.

Drift chambers

The four sets of the BDC's have the same structure, as shown in Figure 2.3. Each set consists of six planes ($xx'uu'vv'$) of sense wires. Each plane has 48 sense wires stretched every 5 mm. Sense wires in x and x' planes are stretched parallel to the vertical axis, while they are tilted by +15 (−15) degree with respect to the vertical axis viewed from the upstream in the u and u' (v and v') planes. Wires in

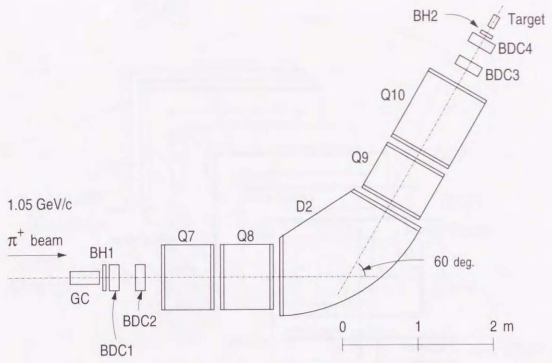

Figure 2.2: *Schematic view of the beamline spectrometer. The Hyperball is not drawn in this figure.*

the x', u' and v' planes are displaced by 2.5 mm with regard to the corresponding wires in the x, u, v planes in order to solve left-right ambiguities.

The cell structure of the chambers is shown in Figure 2.4. Potential wires were placed 2.5 mm away from sense wires and separated the drift cells from each others. We used gold-plated tungsten of $\phi 12$ μm for sense wires, and gold-plated cupper-beryllium of $\phi 75$ μm for potential wires.

Cathod planes were made of Kapton foils of 7.5 μm thick coated with aluminium. We applied −1350 V for the potential wires and −1300 V for the cathod planes. The gas used in those chambers was a mixture of 76% argon, 20% isobutane and ~4% of methylal. The spatial resolution of the BDC's were about 300 μm in r.m.s., and the detection efficiency of each plane was about 99%.

BDC1 and 2 were placed upstream of the spectrometer magnets (QQDQQ), and BDC3 and 4 were placed downstream of the magnets. Momentum of each beam pion was determined by the information from the BDC's in the way explained in Section 3.4.

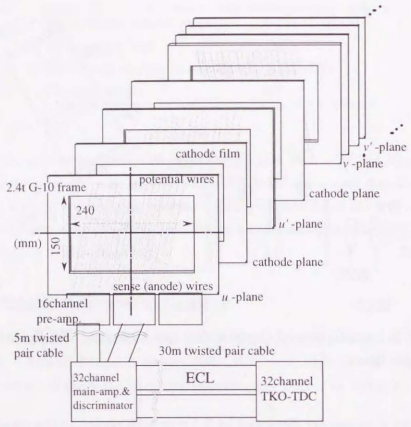

Figure 2.3: *A schematic figure of a BDC and the readout system.*

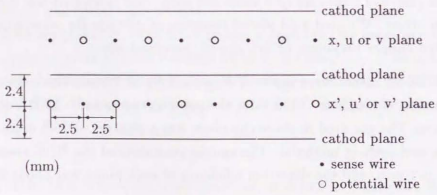

Figure 2.4: *A schematic cross section of a BDC.*

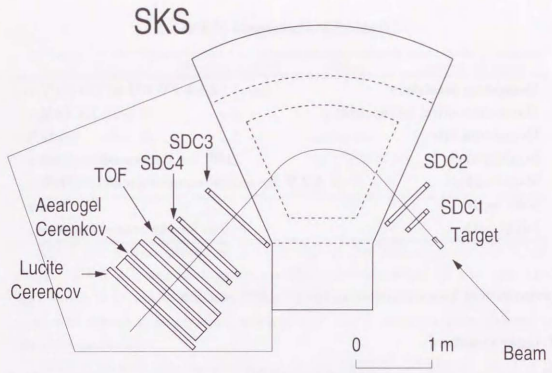

Figure 2.5: *A schematic top view of SKS*

2.2.3 Target

We used a target of ^{7}Li enriched to 98%, which was put in a laminated bag filled with argon gas. The dimensions of the target were 56 mm (width) $\times$ 40 mm (height) $\times$ 250 mm (thickness, corresponding to 13.4 g/cm^2). The target was placed so that the position of the target center was the same as the center of the Hyperball with an accuracy of 3 mm.

2.2.4 Superconducting Kaon Spectrometer (SKS)

Outgoing kaons were identified and momentum analyzed by the Superconducting Kaon Spectrometer (SKS). Figure 2.5 shows the schematic view of SKS and Table 2.2 shows parameters of SKS. SKS consists of a large sector-type dipole magnet, four sets of drift chambers (SDC1-4) and trigger counters.

SKS has a large solid angle of 100 msr, and has a short flight path of $\sim$5 m in order to minimize the kaon decay in flight. These features allow us to efficiently tag hypernuclear production events, which is important for a large γ-ray yield. Central momentum of SKS was set to 0.72 GeV/c since this is a typical

Table 2.2: *Parameters of SKS*

Momentum resolution	0.1% FWHM at 720 MeV/c
Maximum central momentum	1.1 GeV/c
Momentum bite	$\pm$10%
Bending angle	100° for the central trajectory
Magnetic field	2.2 T for central momentum of 720 MeV/c
Solid angle	100 msr
Flight path	$\sim$5 m for the central trajectory

momentum of kaons produced in the (π^+, K^+) reaction.

Trigger counters

Three kinds of trigger counters were used in SKS. First one is called TOF made of 15 segments ($7 \times 100 \times 3$ cm^3 each) of plastic scintillators. TOF counter was used to select kaons from pions and protons by the time-of-flight information between BH2 and TOF in offline analysis (see Section 3.6).

Second one is called AC which consists of two sets (AC1 and AC2) of aerogel Cherenkov counters. Silica aerogel used in AC's has a refractive index of 1.06, which corresponds to threshold momenta of 0.4 GeV/c for pions and 1.8 GeV/c for kaons. Thus AC's were used as veto counters to reject pions at the trigger level.

The last one is called LC which consists of 14 segments ($10 \times 140 \times 4$ cm^3 each) of lucite Cherenkov counters. Lucite has a refractive index of 1.49, and is sensitive to pions (threshold momentum is 0.13 GeV/c) and kaons (threshold = 0.45 GeV/c), but not sensitive to protons (threshold = 0.85 GeV/c). Therefore we can select kaons from protons by requiring a hit in LC at the trigger level.

Drift chambers

Characteristics of the SDC's are shown in Table 2.3. The first two sets of SDC (SDC1 and 2) have basically the same structure as BDC's and were placed just downstream of the target. Differences are that SDC1 has only 4 planes ($uu'vv'$), and that SDC2 has 80 sense wires per a plane instead of 48.

Table 2.3: *Characteristics of the SDC.*

Name	Size(cm^2)	Maximum drift length (mm)	planes	number of sense wires in each plane
SDC1	24×15	2.5	$uu'vv'$	48
SDC2	40×15	2.5	$xx'uu'vv'$	80
SDC3	100×100	2.5	$XX'YY'$	24
SDC4	100×100	2.5	$X \times 6$, $Y \times 6$	24

SDC3 and 4 were placed at the exit side of the SKS magnet. SDC3 has 4 planes ($XX'YY'$), and each plane has 24 sense wires every 42 mm (maximum drift length is 21 mm). Wires in X' and Y' plane were displaced by half cell (21 mm) with regard to corresponding wires in X and Y plane in order to solve the left-right ambiguity.

SDC4 is divided into two chambers, namely SDC4X and SDC4Y. Each of the SDC4 chamber has 6 sense wires per a drift cell. See Figure 2.6 for the structure of drift cells. The maximum drift length of SDC4X and SDC4Y is 21 mm. In order to solve left-right ambiguities, each sense wires were displaced by $\pm$200 μm from the center.

In SDC3 and 4, we have used gold-plated tungsten of ϕ20 μm for sense wires, and gold-plated aluminium of ϕ80 μm for field and shield wires. The gas used for SDC3,4 was a mixture of argon (50%) and ethane (50%).

2.3 Hyperball

Hyperball is a germanium detector system newly constructed for hypernuclear γ-ray spectroscopy experiments. Figure 2.7 shows the schematic view of the Hyperball. In this section, I will describe the components of the Hyperball, namely, germanium detectors, BGO counters and readout electronics.

2.3.1 Germanium detectors

Fourteen coaxial-type germanium detectors are used in the Hyperball. Four are the products of Eurisys Measures company and ten are the products of ORTEC. The dimensions of a germanium detector are shown in Figure 2.8. Each germani-

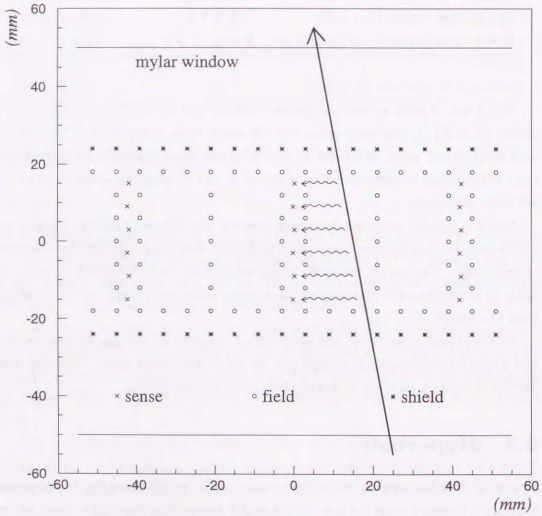

Figure 2.6: *Drift cell structure of SDC4.*

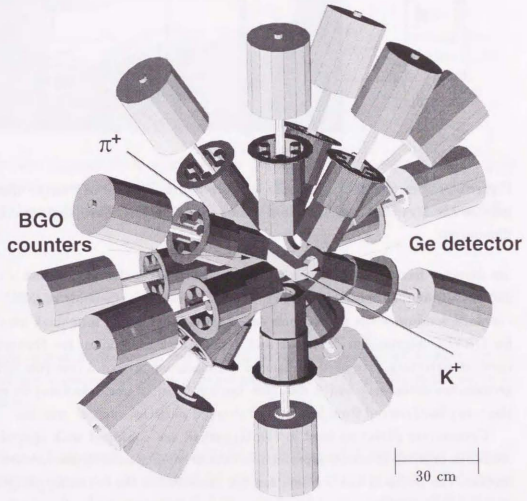

Figure 2.7: *Schematic view of the Hyperball.*

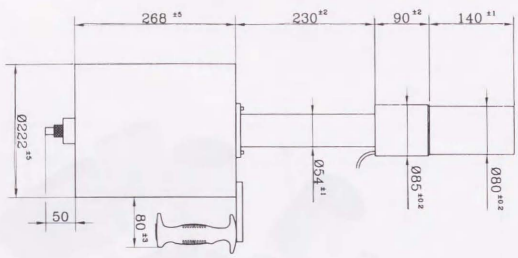

Figure 2.8: *Dimensions of a coaxial type germanium detector of Eurisys Measures used in the Hyperball. Germanium detectors of ORTEC have slightly different dimensions.*

um detector has a high-purity, n-type crystal of which effective volume is about 250 cm^3 (about 70 mm$\phi \times$ 70 mm), and has a relative efficiency of 60%[1]. The entrance window of the germanium detectors is made of 0.5 mm thick beryllium for ORTEC germanium detectors and 1 mm thick aluminium for Eurisys germanium detectors. We used additional aluminium plates of 3 mm (for ORTEC germanium detectors) and 2 mm (for Eurisys germanium detectors) to reduce the γ-ray background from low-energy charged particles such as protons.

Germanium detectors used in the Hyperball are equipped with special electronics in order to minimize a problem occurs in conditions of hypernuclear experiments. The problem and our solution are described in the following paragraphs.

Difficulties of using germanium detectors in hypernuclear experiments

As described in Section 1.3, there was only one experiment which used germanium detectors for hypernuclear study. This is mainly becase it is very difficult to operate germanium detectors in conditions of hypernuclear experiments, as described below.

We usually use meson beams such as π^+ or K^- to create hypernuclei. Though

[1]Normalization standard is an NaI counter of 3"$\phi\times$3".

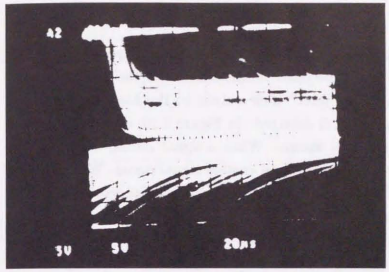

Figure 2.9: *Signals from a germanium detector with resistive-feedback type preamplifier operated in π^+ beam at KEK-PS K6 beamline. When the output of the preamplifier is saturated , baseline of the following shaping amplifier shifts.*

a typical rate of meson beams is a few million particles per second at most, which is quite low compared to primary beam experiments, the quality of the beam is a problem.

When a high-energy charged particle passes through a germanium detector, the energy deposit is an order of 50 MeV even if the particle is a minimum ionizing particle. This is extremely large compared to the energies of the γ-rays to be measured, and such large pulses often cause overload of preamplifiers. If the preamplifiers are resistive feedback type ones that release collected charges through resistors, this results in a large baseline shift due to mismatch of pole-zero cancellation in main amplifiers, as shown in Figure 2.9. The deadtime caused by the baseline shift is typically several hundred microseconds. In the case of the present experiment, the penetrations of charged particles happen at a rate of about 10^4 times per second. Therefore, usual germanium detectors with resistive feed-back type preamplifiers are useless in hypernuclear experiments.

Solution in Hyperball

In hyperball, this difficulty was solved by using transistor-reset type preamplifiers instead of resistive feed-back type ones. Characteristic of the transistor-reset type preamplifiers is that they "reset" their output to the baseline level when an overload of the output signal is detected. In Figure 2.10, conceptual output of a preamplifier of such type is shown. When a signal comes, output of the preamplifier rises, and keeps that level until another signal comes. When a signal make the output higher than a threshold level, the preamplifier resets the output to the baseline by discharge, before it is saturated. Reset procudure takes only a few microseconds in the case of our germanium detectors, and the total deadtime including that of following main amplifier can be very short as ~ 20 μs per reset. In the present experiment, a typical deadtime due to reset was as small as $\sim 20\%$, for a typical reset rate of $\sim 1 \times 10^4$ per second.

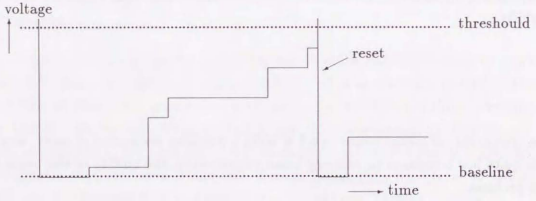

Figure 2.10: *Conceptual illustration of output signal of a reset-type preamplifier.*

The preamplifiers are commercially available, but the gain of our preamplifiers were lowered by a factor of three in order to reduce the reset rate. The threshold level for reset was 10 V, which corresponds to 150 MeV signal in the case of our preamplifiers.

Another important electronics to reduce the in-beam deadtime is a shaping amplifier of gated integration type. We used ORTEC 973U (Ultra-Highrate Amp., UHA), of which deadtime due to pileup is small (6 μs per a signal). It is noted that the energy resolution obtained with an UHA is worse only by $\sim 20\%$ than the best resolution achievable with the germanium detector.

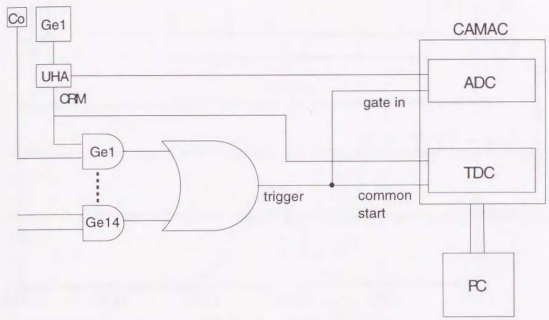

Figure 2.11: *Block diagram for triggering and data acquisition of the monitoring system.*

2.3.2 Online monitoring system and in-beam performances of germanium detectors

The in-beam performances of the germanium detectors were monitored by the online monitoring system. We used a simple, CAMAC-based DAQ system which is independent of the main DAQ system for the monitoring system.

Figure 2.11 shows the block diagram for the online monitoring system. A weak (~ 1 kBq) source of ^{60}Co was placed near each of the germanium detectors (see Figure 2.14). ^{60}Co sources were embedded in plastic scintillators, which detect β-rays from ^{60}Co decay. By taking the coincidence between the germanium detectors and the ^{60}Co sources, ^{60}Co γ-rays were selected.

The ADC data were taken for the same duration (~ 0.5 s per a 3 second cycle) in the beam-on period and in the beam-off period. Figure 2.12 shows the γ-ray spectra around the 1.33 MeV peak for a typical germanium detector. We can see the effect of high counting rate by comparing those two spectra as;

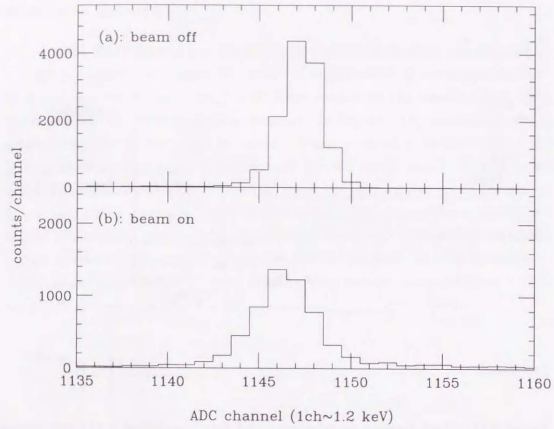

Figure 2.12: *γ-ray energy spectra around the 1.33 ^{60}Co peak for a typical germanium detector. The effect of in-beam high counting-rate can be seen.*

- The peak position in the beam on spectrum shifts by $-1 \sim -2$ keV from that in the beam off spectrum.
- The peak width is broadened slightly with beam on. The energy resolution for a typical germanium detector was 3.0 keV FWHM with beam off, and 3.5 keV FWHM with beam on.
- In-beam deadtime was obtained by comparing the yields with beam on and off. In-beam deadtime averaged over the fourteen germanium detectors and whole beamtime was $46.2 \pm 0.5\%$

A typical couting rate of a germanium detector was about 4×10^4 counts per second for a typical beam intensity of 1.8×10^6 pions per spill on the experimental target. Position dependence of the counting rate due to pion scatterings at the target was observed. Because of this effect, a typical deadtime of a germanium

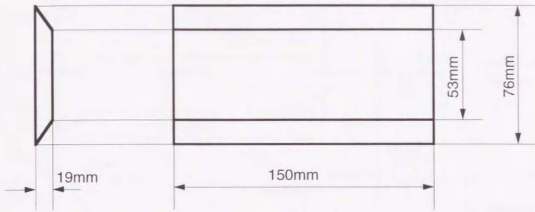

Figure 2.13: *Dimension of a BGO crystal. Six crystals are used for one germanium detector.*

detector in downstream positions was 55%, while that in upstream positions was 40%.

2.3.3 BGO counters

We used bismuth germanate ($Bi_4Ge_3O_{12}$, BGO) scintilation counters to suppress γ-ray background in germanium detectors from Compton scattering and high-energy γ-rays from π^0's. BGO was chosen for this purpose because of a good suppression efficiency for γ-rays. Dimensions of a BGO crystal are shown in Figure 2.13. Thickness of the BGO counters was chosen to be 19 mm from the available space in the hyperball and the budget constraint.

Six pieces of BGO counters were used for each germanium detector. Schematic drawings of a set of six BGO and one germanium detector are shown in Figure 2.14. The six BGO crystals of a set were placed in the same housing, partitioned by teflon sheets. One $1\frac{1}{8}$ inch PMT (HAMAMATSU R1355) was used to extract signals from each BGO crystal. The inner wall of the housing was made of 1 mm thick aluminium to avoid absorbtions of scattered γ-rays in the wall. The outer wall of the housing was made of iron which is used as a magnetic shield as well as a support.

Energy resolution of BGO counters was typically 25% (FWHM) for 662 keV γ-rays of ^{137}Cs, and a typical timing resolution was 4 ns (FWHM) for a γ-ray energy of around 1 MeV. In order to make the suppression efficiency higher, the threshold of the discriminators for the BGO counters were determined so that single photon events can be discriminated (typically $V_{\rm th} = 25$ mV for single

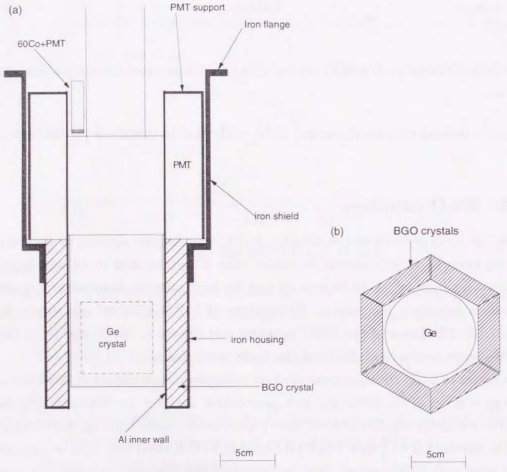

Figure 2.14: *A set of germanium detector with six BGO counters and a ^{60}Co source (embedded in plastic scintillator). (a): Cross-section. (b): View from below.*

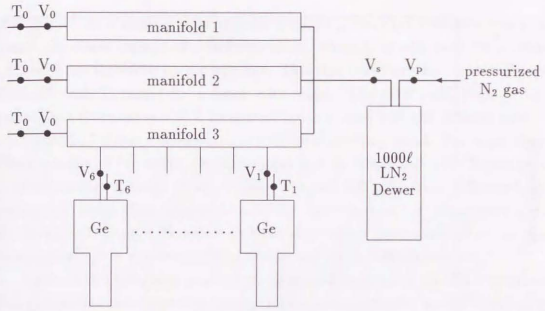

Figure 2.15: *Schematic diagram of the LN_2 auto-supplier system.*

photon signal of 50 mV). A typical counting rate of a BGO counter was 50 kHz in beam with this threshold level.

2.3.4 Liquid nitrogen auto-supplier system

The germanium detectors were fed with liquid nitrogen (LN_2) by an auto-supplier system once per day. Figure 2.15 shows a schematic diagram of the system. There were three manifolds in the system, each of them can supply up to six germanium detectors with LN_2. Those three manifolds can be controlled independently by the programmable controller or manual operation.

The auto-filling procedure can be initiated either by the preset timer or by pushing the start button manually at the control panel. This opens the V_s and V_p valves which are common to all the three manifolds and the V_0 valve of the manifold. The 1000 liter LN_2 Dewer is pressurized by nitrogen gas comes via the V_p valve and LN_2 flows through the V_s valve to the manifold. When the temperature of the manifold measured by the T_0 thermometer reaches the LN_2 temperature (77 K), V_0 automatically closes and the valves to the germanium detectors (V_1 to V_6) open. When the Dewer of a germanium detector is full and LN_2 pours out of it, the thermometer (T_1 to T_6) detects it and the controller closes the corresponding valve. If all the Dewers are full, the controller finishes

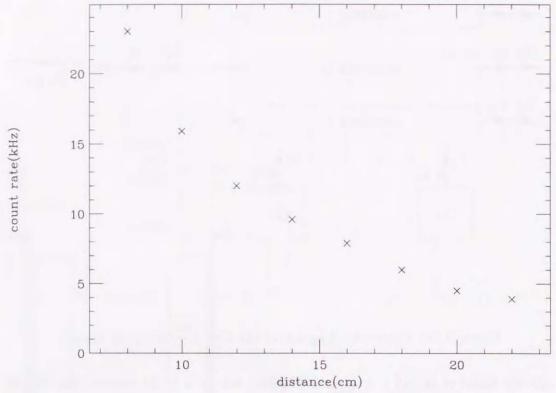

Figure 2.16: *Beam halo rate as a function of the distance from the beam at the target point measured by a plastic scintilation counter.*

the whole process by closing the V_s and V_p valves. For safety, the remaining LN_2 in the manifold is exhausted via the V_0 valve for five minuites after the end of procedure.

2.3.5 Arrangement of germanium detectors

Considering the in-beam deadtime and possible radiation damage, it is better to place germanium detectors so as to make the rate of beam halo particle penetration as small as possible. To determine the positions of the germanium detectors, we studied the beam halo rate by using a plastic scintilator which has the same cross section as the germanium detectors viewed from the beam. Figure 2.16 shows the counting rate of the scintilation counter as a function of the distance from the beam at the target point.

In order to keep a large solid angle with a moderate particle penetration rate, we placed the germanium detectors so that the distance from the beam line center

was 15 cm. As a result, the arrangement of the germanium detectors was in a barrel like shape instead of a ball like shape which is usually used for normal nuclear γ-ray spectroscopy experiments. This shape also matches with the very thick (25 cm) Li target for a large solid angle. The total solid angle of the germanium detectors was 15% for a point γ-ray source with this arrangement.

Figure 2.17 shows a schematic view of the supporting stand. The supporting stand consists of two parts: the upper part and the lower part. The upper part is an aluminium cylinder, of which dimensions are 660 mmϕ times 510 mm long. Figure 2.18 shows the schematic view of the upper part of the supporting stand. As shown in the figure, there are eighteen slots where germanium detectors can be attached, six in upstream, six in middle and six in downstream side.

Figure 2.19 shows how a set of germanium detector and six BGO counters was attached to the supporting frame. A germanium detector was fixed by being sandwiched between two aluminium disks, and the disks and BGO counters were connected to the flange by six screw bars used as bolts and nuts. The distance between a germanium detector and the beam was 15 cm, which can be adjusted by moving the screw bars. It is noted that germanium detectors and BGO counters can be attached to the stand without the others, and can be moved independently. The BGO counters were placed so that their surface was by 2 cm nearer to the beam than that of germanium detectors.

Since we had only fourteen germanium detectors, four slots must be empty. We chose to leave four of the downstream slots to be empty, since germanium detectors in downstream slots suffer from higher counting rate due to reactions at the target.

2.3.6 Readout electronics

Figure 2.20 is the block diagram of the electronics for germanium detectors. Output of the preamplifiers embedded in the germanium detectors went to main amplifiers (UHA). The outputs of the UHA were sent to an ADC of the main DAQ system (ORTEC AD413a) and that of the monitoring system.

Timing signals were also taken from the UHA with the CRM (count rate meter) output. Timing filtering amplifiers (TFA) were not used because they didn't work well. A pipelined multihit TDC (LeCroy 3377) was used to take timing data. This TDC was also used for pileup rejection utilizing the multihit feature. Reset timing of the preamplifiers was also recorded by the TDC to reject

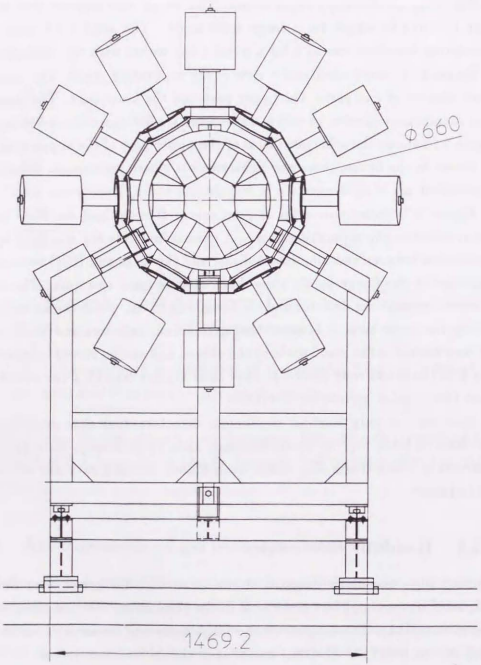

Figure 2.17: *View of the whole stand with germanium detectors from upstream of the beam.*

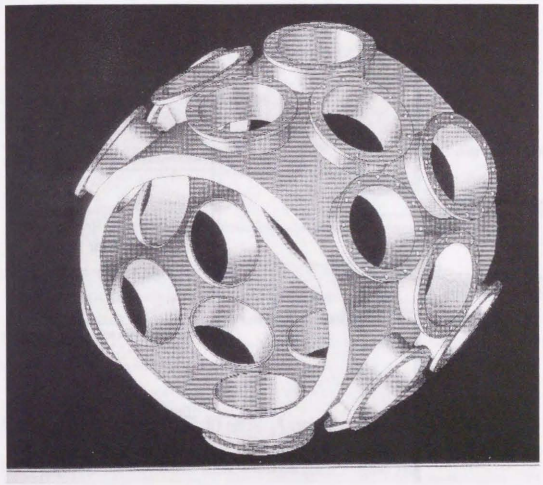

Figure 2.18: *Schematic view of the upper part of the supporting stand.*

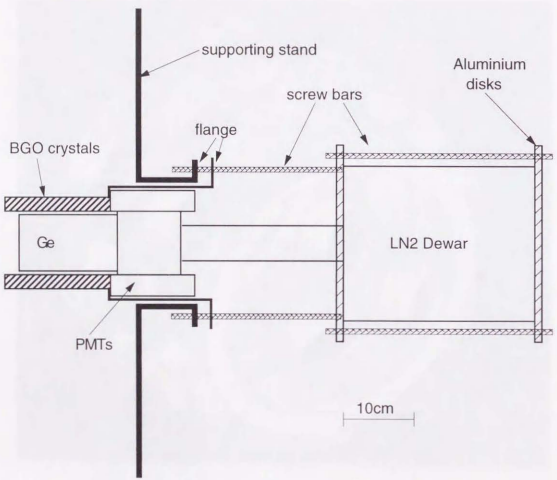

Figure 2.19: *schematic view of the connection between the stand and a set of a germanium detector and BGO counters.*

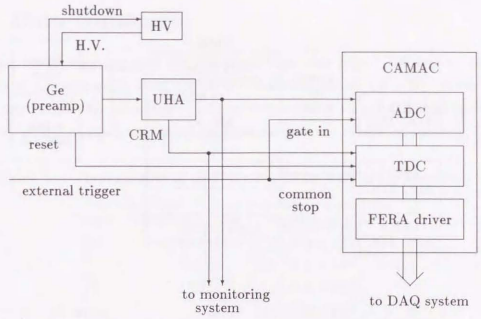

Figure 2.20: *Block diagram of readout electronics of germanium detectors.*

events occurred just after the reset of preamplifiers.

Those electronics other than preamplifiers of germanium detectors were placed in a temperature-controlled hut to avoid gain drift of UHA and ADC.

Signals of BGO counters were read out by charge-sensitive ADC's and TDC's in the same way as other counters.

2.4 Trigger and Data Acquisition System

For triggering, first we made BEAM trigger for π^+ beam as;

$$\text{BEAM} = \overline{\text{GC}} \cdot \text{BH1} \cdot \text{BH2}.$$

As mentioned in Section 2.2.2, positron contamination in the beam was rejected by GC veto, and proton contamination was rejected by the coincidence timing of BH1 and BH2 at this level. Contamination of K^+ in the beam was small and can be removed in the offline analysis (see Section 3.2).

Outgoing kaons were selected by the KOUT trigger as;

$$\text{KOUT} = \text{TOF} \cdot \text{LC} \cdot \overline{\text{AC1}} \cdot \overline{\text{AC2}},$$

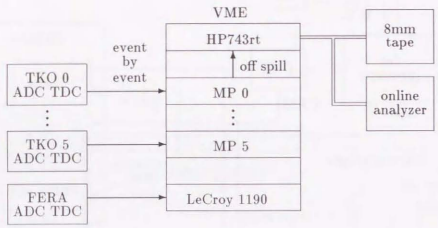

Figure 2.21: *Schematic diagram of the data acquisition system.*

where LC was used to reject protons, and AC's were used to reject pions, as explained in Section 2.2.4.

Thus, the main trigger for the (π^+, K^+) reaction (PIK) was determined by;

$$\text{PIK} = \text{BEAM} \cdot \text{KOUT}.$$

Typical trigger rate was 300/spill, most of which were protons contaminating in the outgoing kaons[2]. We did not use germanium detectors nor BGO counters in the trigger so that inclusive ^{7}Li(π^+, K^+) reaction spectrum can be taken.

A schematic diagram of the data acquisition system is shown in Figure 2.21. All the ADC and TDC data except for those of germanium detectors were collected via six TKO crates to the corresponding MP (Memory Partner) module in the VME crate. ADC and TDC data of germanium detectors were collected via FERA bus to the VME memory module (LeCroy 1190). The host computer (HP743rt) in the VME crate read the data out from the memory modules once per spill during the beam-off period.

The data were processed by the host computer and were written on 8mm tapes. Most of them were also sent to neibouring computers for online analysis. We have used a Linux PC and a HP workstation for that purpose.

[2]LC has small, but not negligible efficiency for protons due to δ-rays.

2.5 Data summary

The total beam time we used for the experiment was about 700 hours, most of which were executed in June 1998. We irradiated about 1.0×10^{12} pions on the lithium target. We also took reference data without target and with carbon targets. Number of pions irradiated on those targets are tabulated in Table 2.4.

Table 2.4: *Total number of pions irradiated on each of the target.*

Target	thickness (g/cm^2)	number of pions
^{7}Li	13.4	1.0×10^{12}
C	5.2	1.4×10^{10}
C	13.7	1.3×10^{10}
empty	—	1.3×10^{10}

Chapter 3

Analysis I – the (π^+, K^+) reaction

The analysis procedures can be divided into two parts, namely, the analysis of the (π^+, K^+) reaction and the analysis of γ-rays. In this Chapter, I will describe about the analysis of the (π^+, K^+) reaction and the selection of the bound states of ${}^{7}_{\Lambda}$Li. In the next Chapter, I will describe about the analysis of γ-rays.

3.1 Overview of the analysis of the (π^+, K^+) reaction

Analysis of the (π^+, K^+) reaction was done in the following procedure.

1. **Selection of real π^+ beam events.**

   Accidental coincidence of BH1 and BH2 in the beam trigger was removed. Small kaon contamination in the beam was also removed at this level.

2. **Rough selection of outgoing K^+.**

   By checking the data of TOF and LC, most of the proton contamination in the outgoing particles was rejected.

3. **Determination of π^+ momentum.**

   The BDC data were analyzed to reconstruct the pion momentum and trajectory.

4. **Determination of momentum of outgoing particle**

   Momentum and trajectory of the outgoing particles were determined by the SDC data.

5. **Selection of outgoing K^+.**

   Velocity of an outgoing particle was determined by TOF data and the flight path length of the particle. Mass of the outgoing particle was determined by momentum and velocity, and real K^+ events were selected.

6. **Reconstruction of reaction angle and vertex point**

   Reaction angle and vertex point were calculated by the tracking data.

7. **Reconstruction of missing mass**

   From the obtained momemta of pion and kaon, missing mass for ${}^{7}_{\Lambda}$Li was reconstructed. Bound state production of ${}^{7}_{\Lambda}$Li can be selected by the missing mass cut.

Those procedures are explained in detail in the following sections.

3.2 Selection of real π^+ beam events

Figure 3.1 shows the time-of-flight spectrum between BH1 and BH2. In order to remove accidental coincidence background and kaon contamination in the beam, we applied a cut to the spectrum as shown in the figure.

3.3 Rough selection of outgoing K^+

Although kaons can be almost perfectly identified after the tracking procedure as explained in Section 3.6, the tracking analysis of SDC data requires much CPU time. Rough selection is useful to reduce CPU time by rejecting proton contamination.

We used TDC of TOF and LC for the rough selection. Figure 3.2 shows scatter plots of TOF-TDC versus LC-TDC, before and after the kaon selection described in Section 3.6. We applied a cut so as not to lose real K^+ events as shown in the figure.

3.4 Determination of π^+ momentum

Momentum and trajectory of the beam pion were determined in the following way;

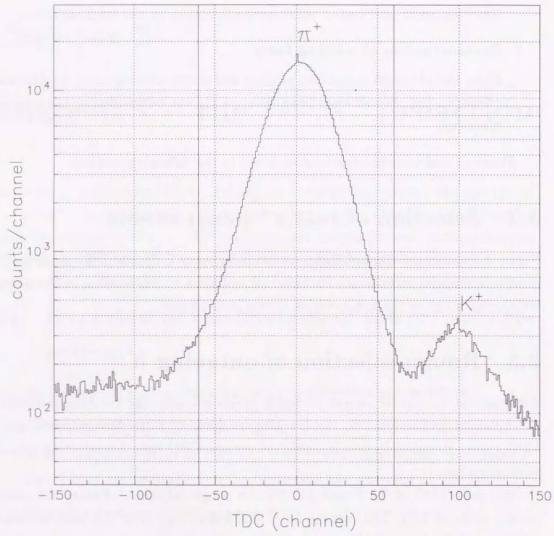

Figure 3.1: *Time-of-flight between BH1 and BH2. Events in the region enclosed by the solid lines were accepted as good pion events.*

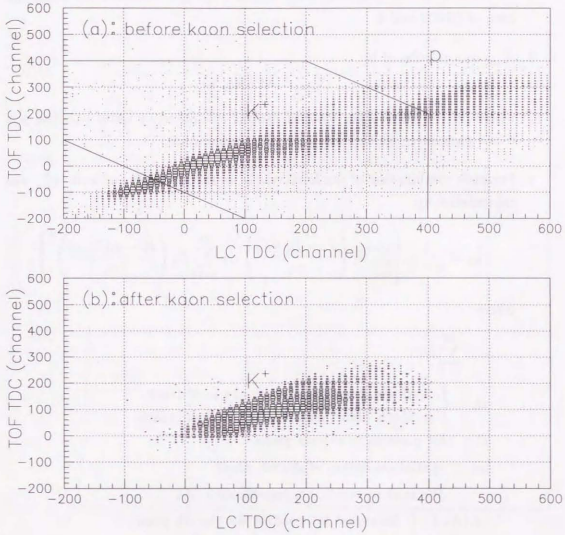

Figure 3.2: *Scatter plot of TOF-TDC versus LC-TDC before and after kaon selection described in 3.6. Cut condition for rough kaon selection is shown by the solid lines in the figure.*

1. At the entrance of the beam line spectrometer magnets, local tracks were searched for by linear fitting of the hit positions in BDC1 and 2. A parameter set of two independent positions and two independent angles, $\vec{X}_{\rm in}$, was determined for each local track.

2. At the exit of the magnets, local tracks were also searched for using the data of BDC3 and 4.

3. $\vec{X}_{\rm out}$ was calculated by

$$\vec{X}_{\rm out} = \mathcal{M}\left(\vec{X}_{\rm in}, p\right),$$

where $\mathcal{M}$ is a third order transfer matrix calculated by Orbit [33] and p is a free parameter which represents pion momentum.

4. For each combination of the local tracks at the entrance and exit, $\chi^2_{\rm K6}$ was caluculated by;

$$\chi^2_{\rm K6} \equiv \frac{1}{n-5}\left\{\sum_{i=1}^{12} H_i\left(\frac{P_i - f_i(\vec{X}_{\rm in})}{w_i}\right)^2 + \sum_{i=13}^{24} H_i\left(\frac{P_i - g_i(\vec{X}_{\rm out})}{w_i}\right)^2\right\},$$

where

$n = \sum_{i=1}^{24} H_i$

$H_i = \begin{cases} 1 & \text{if } i\text{th plane has a hit in the local track.} \\ 0 & \text{if } i\text{th plane has no hit in the local track.} \end{cases}$

P_i : hit position in the ith plane.

w_i : spatial resolution of the ith plane.

We took $w_i = 0.3$ mm independent of i.

$f_i(\vec{X}_{\rm in})$, $g_i(\vec{X}_{\rm out})$: Expected hit position for the ith plane, calculated by $\vec{X}_{\rm in}$ and $\vec{X}_{\rm out}$.

5. The best track combination and pion momentum were determined so as to give the smallest $\chi^2_{\rm K6}$.

Figures 3.3 and 3.4 show the distribution of minimum $\chi^2_{\rm K6}$ and pion momentum thus obtained for a typical run, respectively.

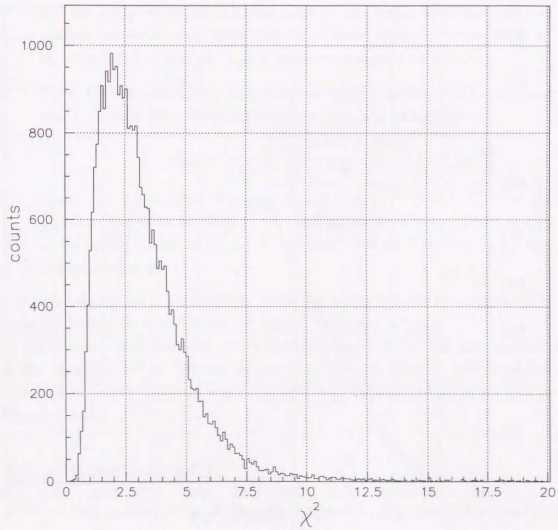

Figure 3.3: *Minimum $\chi^2_{\rm K6}$ distribution for a typical run.*

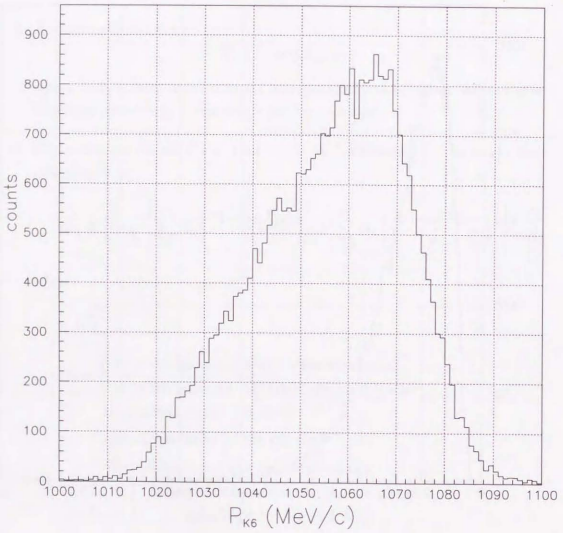

Figure 3.4: *Momentum distribution of the beam pion.*

3.5 Determination of momentum of outgoing particle

Momentum and trajectory of the outgoing particle were determined from SDC data in the following way.

1. For a set of five free parameters, — a momentum, two independent positions and two independent angles at the target — the trajectory of the scattered particle was determined by solving the equation of motion numerically by the Runge-Kutta method using a measured magnetic field map.

2. Those five parameters were determined so that the chi-square of the tracking was minimized. The tracking chi-square, $\chi^2_{\rm SKS}$ was defined by

$$\chi^2_{\rm SKS} = \frac{1}{n-5}\sum_{i=1}^{n}\left(\frac{x_i^{\rm tracking} - x_i^{data}}{w_i}\right)^2,$$

where n is the number of planes having hits, $x_i^{\rm tracking}$ and $x_i^{\rm data}$ are hit positions on the ith hit plane in the tracking and data, respectively, and w_i is the spatial resolution of the ith hit plane and was taken to be 0.3 mm independent of i.

Figure 3.5 shows the χ^2 distribution, which has a long tail due to decay-in-flight events of kaons. We accept events of $\chi^2_{\rm SKS} < 30$ as good events.

Since there are systematic errors in the magnetic field map and positions of the chambers, the momentum calculated in this way must be calibrated and corrected for such systematic errors. Correction of the momentum is desribed in Section 3.8.1.

3.6 Selection of K^+

After the SKS tracking, mass of the outgoing particle, $M_{\rm out}$, was calculated by;

$$M_{\rm out} = \frac{p}{\beta}\sqrt{1-\beta^2},$$

where p and β are momentum and speed of the outgoing particle, respectively. β was determined from time-of-flight information from BH2 to TOF and the path length from the target to TOF calculated from the trajectory. Figure 3.6 shows the spectrum of the outgoing particle mass. Events with 350 MeV $< M_{\rm out} <$ 650 MeV were accepted as good events.

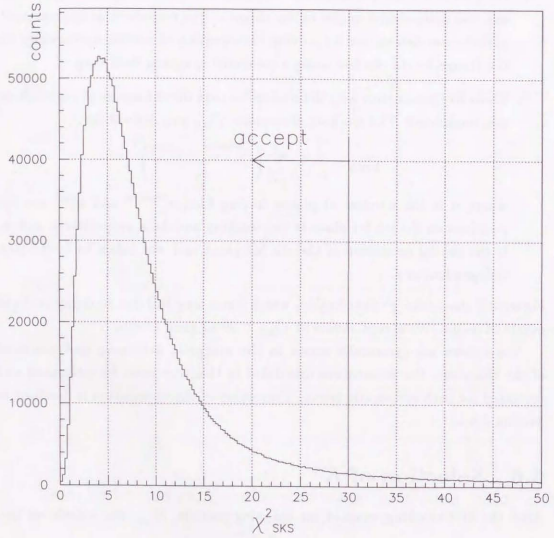

Figure 3.5: *Minimum χ^2_{SKS} distribution.*

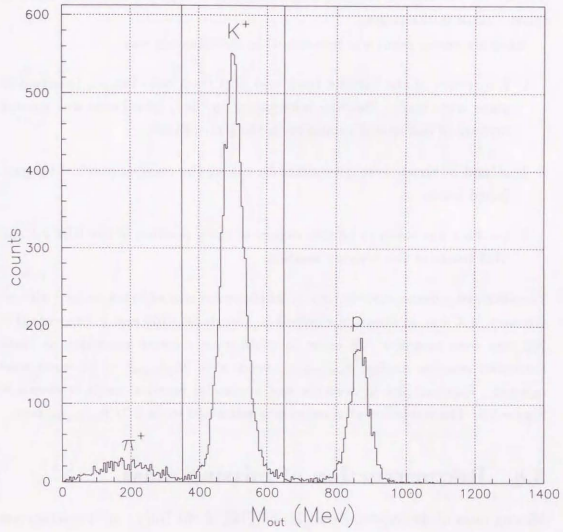

Figure 3.6: *Mass distribution of the outgoing particle.*

3.7 Reaction angle and reaction vertex point

Reaction angle was determined by the local track of the beam pion determined by BDC3 and 4 and the trajectory of the outgoing particle. Figure 3.7 shows the distribution of the reaction angle for the ^{7}Li(π^+, K^+) events. Angular resolutions were estimated to be 8 mrad (r.m.s) for the horizontal reaction angle and 10 mrad (r.m.s.) for the vertical reaction angle including a multiple scattering effect of about 7 mrad in the target.

Reaction vertex point was determined in the following way;

1. Projections of the BDC3,4 track and SKS track onto the x-z (horizontal) plane were made. Position information in the y coordinate was ignored because of bad spatial resolution in the y coordinate.

2. x- and z- vertex were determined by taking the crossing point of the projected tracks.

3. y-vertex was taken to be the average of the y position of the BDC3,4 and SKS tracks at the z-vertex position.

The obtained z-vertex distribution, of which center was adjusted to zero with an accuracy of 4 mm, is shown in Figure 3.8. Events of -160 mm $< (z-\text{vertex}) <$ 160 mm were accepted. In order to avoid poor z-vertex resolution at small horizontal reaction angles ($\theta_{\text{horizontal}}$), events with $|\theta_{\text{horizontal}}| < 10$ mrad were rejected. Contour plot of z-vertex and horizontal reaction angle is shown in Figure 3.9. The resolution of z-vertex was estimated to be $1.2/|\theta_{\text{horizontal}}|$ mm.

3.8 Reconstruction of missing mass

Missing mass of the hypernucleus $^7_\Lambda$Li, $M(^7_\Lambda\text{Li})$, in the ^{7}Li(π^+, K^+) reaction was calculated by

$$M(^7_\Lambda\text{Li}) = \sqrt{(E_\pi + M(^7\text{Li}) - E_K)^2 - (p_\pi^2 + p_K^2 - 2p_\pi p_K \cos\theta)}, \qquad (3.1)$$

where E_x and p_x are energy and momentum of a particle x, $M(^7\text{Li})$ is the mass of the ^{7}Li target nucleus, and θ is the reaction angle. Note that missing mass spectra in the figures below are plotted in the scale of $M(^7_\Lambda\text{Li}) - M(^7\text{Li})$.

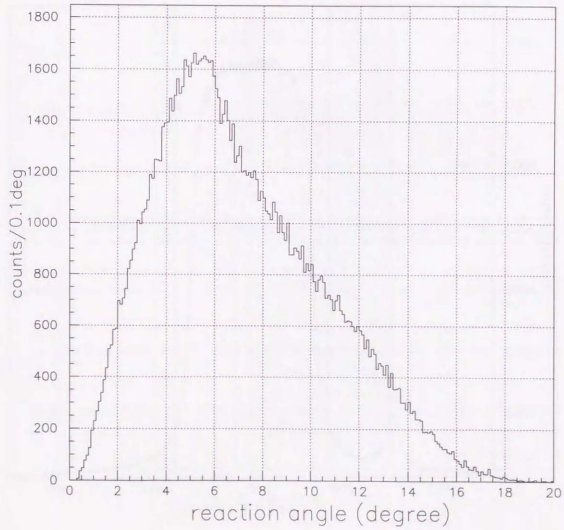

Figure 3.7: *Reaction angle distribution of the* ^{7}*Li*$(\pi,^+, K^+)$ *reaction.*

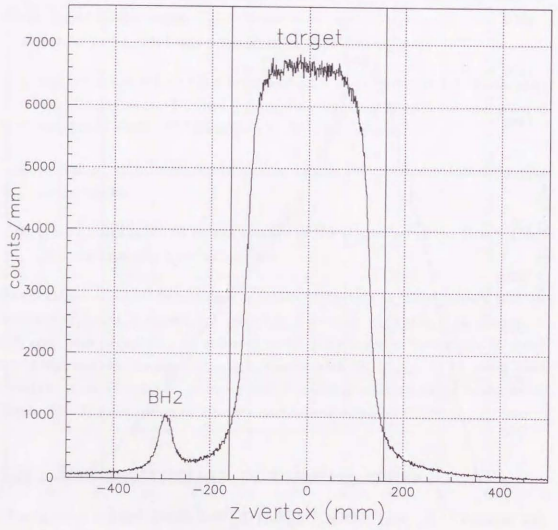

Figure 3.8: *Reaction z-vertex distribution.*

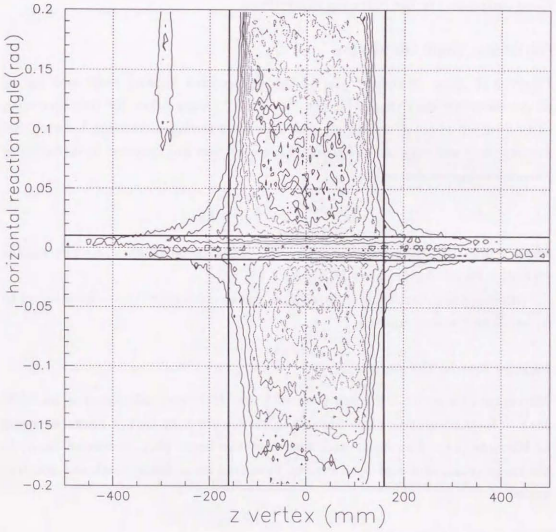

Figure 3.9: *Contour plot of reaction z-vertex versus horizontal scattering angle. See text for the cut conditions represented by the solid lines.*

3.8.1 Momentum correction

Before obtaining missing mass spectrum, the momenta of pions and kaons determined by the procedures explained in the sections above should be corrected for the systematic errors caused by uncertainty of the magnetic fields and position of the chambers. Energy loss in the target was also corrected for. I will describe those corrections in the following subsections.

Horizontal angle correlation

Figure 3.10 shows a scatter plot of the uncorrected missing mass and $\mathrm{d}x/\mathrm{d}z$ of the outgoing kaon (u_{SKS}) for the $^{12}\mathrm{C}(\pi^+, K^+)$ data taken for reference with carbon target of 5.4 g/cm^2 thick. One can see a strong correlation between the missing mass and u_{SKS} in the figure. This correlation was removed by introducing phenomenological correction

$$p_K^{\mathrm{corrected}} = p_K + c \cdot u_{\mathrm{SKS}},$$

where c is a correction parameter and was taken to be 20 MeV/c. The scatter plot after correction is shown in Figure 3.11.

Other correlations, such as $\mathrm{d}y/\mathrm{d}z$ and higher order correlations were found to be small and were neglected.

Energy loss in the target

Momentum losses for a lithium plate of 1 cm thick were calculated to be 0.891 MeV/c for 1.05 GeV/c pions and 1.281 MeV/c for 0.72 GeV/c kaons by using LEPS code [34]. The flight path length of the beam pion (scattered kaon) in the target was calculated by using the measured pion (kaon) track and reaction vertex.

Calibration of the absolute scale

Figure 3.12 shows the obtained missing mass spectrum after the corrections described above. In order to extract the position of the ground state, the spectrum was fitted with (4 gaussians) + (Quasifree continuum) + (constant background). Fitting parameters for the four gaussians are summarized in Table 3.1. Relative heights of the four gaussians were taken from the result of the previous SKS experiment which were performed with the same conditions but with a thin

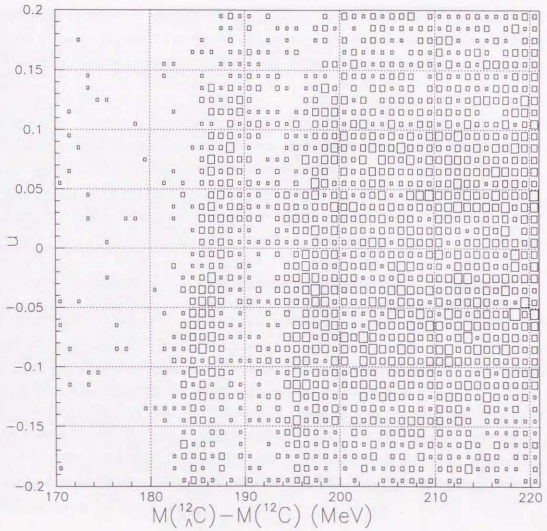

Figure 3.10: *Correlation between horizontal angle and the missing mass before the horizontal angle correction.*

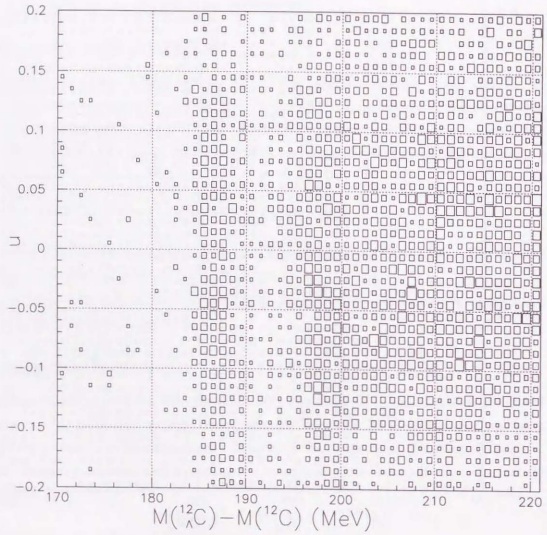

Figure 3.11: *Correlation between horizontal angle and the missing mass after the horizontal angle correction.*

(1.4 g/cm^3) target [35] and were fixed to be 0.23:0.26:0.14:0.09. Relative positions of the four gaussians were also fixed to be E_x =0.0, 2.05, 4.28 and 6.0 MeV from the present result (for the second gaussian, see Section 5.3.1) and Ref. [35] (for the third and fourth gaussians). Quasifree continuum shape was assumed to be proportional to $\sqrt{E_x - 5.58}$ where E_x was measured in the unit of MeV, and height of the continuum was a free parameter. Mass resolution was a free parameter common to all the gaussian peaks and quasifree continuum. The result of the fitting is shown in the figure. Mass resolution was obtained to be 4.2 MeV (FWHM), which is consistent with an estimation of energy loss fluctuation in the target.

Table 3.1: *Fitting parameters of the four gaussians. Number of events in each peak is also shown from the result of the fitting.*

gaussian	main component	E_x (MeV)	rel. peak height	number of events
#1	$1/2^+$	0.0 (fixed)	0.23 (fixed)	2.98×10^4
#2	$5/2^+$	2.05 (fixed)	0.26 (fixed)	3.36×10^4
#3	$1/2^+(T=1)$	4.28 (fixed)	0.14 (fixed)	1.81×10^4
#4	$5/2^+(T=1)$	6.0 (fixed)	0.09 (fixed)	1.16×10^4

To reproduce the correct binding energy of the ground state (5.58 MeV [36]), momenta of pion and kaon were adjusted by +4.0 MeV/c and −4.8 MeV/c, respectively. This adjustment is arbitrary, because one can also reproduce the same effect by chaging either pion momentum by +8.0 MeV/c or kaon momentum by −9.6 MeV/c instead of changing both momenta of pion and kaon. Therefore, absolute momentum scale has still some uncertainty. The effect of this uncertainty is discussed in Section 5.3.2.

3.8.2 Binding energy of Λ

After the corrections described above, missing mass of ${}^7_\Lambda$Li was converted to the binding energy of Λ (B_Λ) by

$$-B_\Lambda = M({}^7_\Lambda\mathrm{Li}) - M_\Lambda - M({}^6\mathrm{Li}),$$

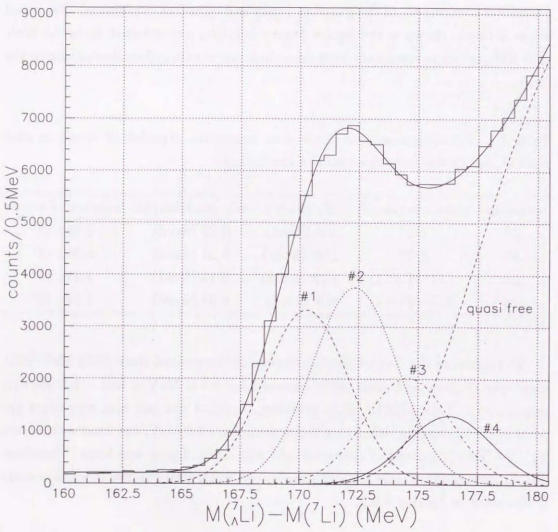

Figure 3.12: *Missing mass spectrum of ${}^{7}_{\Lambda}$Li. The abscissa is plotted in the scale of $M({}^{7}_{\Lambda}\mathrm{Li}) - M({}^{7}\mathrm{Li})$. Lines show the result of the fitting.*

where M_Λ and $M({}^{6}\mathrm{Li})$ are the mass of Λ and ^{6}Li core nucleus[1], respectively. Figure 3.13 shows the mass spectrum of ${}^{7}_{\Lambda}$Li in the scale of $-B_\Lambda$. The region, -10 MeV $< -B_\Lambda < 2$ MeV was selected as the bound state region of Λ particle.

[1] We assumed that the ^{6}Li core is in the ground state.

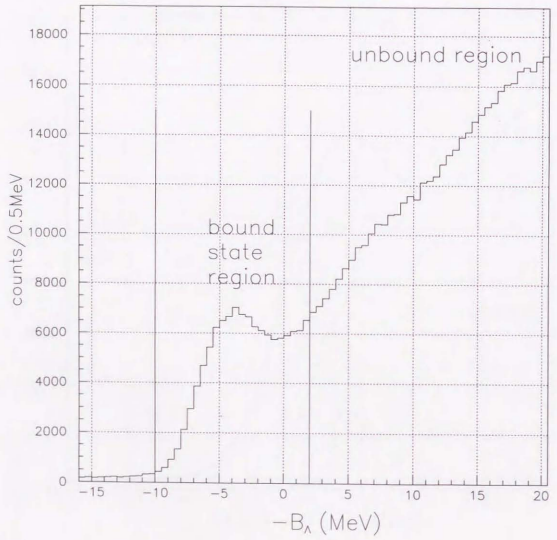

Figure 3.13: *Spectrum of the binding energy of the* Λ. *We have selected* -10 MeV $< -B_\Lambda < 2$ MeV *as the bound state region.*

Chapter 4

Analysis II – γ-rays

4.1 Event selection

We have selected events in which any one of germanium detectors had a good hit and there were no hits in the corresponding six BGO counters. How a good germanium hit and BGO hits were selected is described in the following subsections.

4.1.1 Germanium detector

A good hit in a germanium detector was selected in the following way;

1. **ADC cut**

   Overflows and underflows in ADC were rejected.

2. **TDC cut**

   Figure 4.1 shows a plot of ADC versus TDC for a typical germanium detector. We set the TDC cut gate for each germanium detector as a function of ADC. Figure 4.2 shows TDC gate widths for several ADC ranges of a typical germanium detector. We set the gate width so as to make the event loss due to this cut is less than 5%. The width of the gate as a function of ADC for a typical germanium detector is shown in Figure 4.3.

   If there were more than one TDC hits in the same germanium detector, any one of the hits must fulfill the condition.

3. **Pileup rejection**

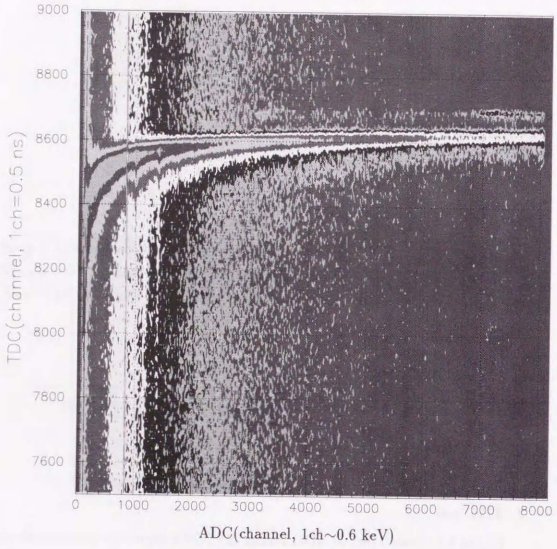

Figure 4.1: *ADC-TDC relation of a typical germanium detector.*

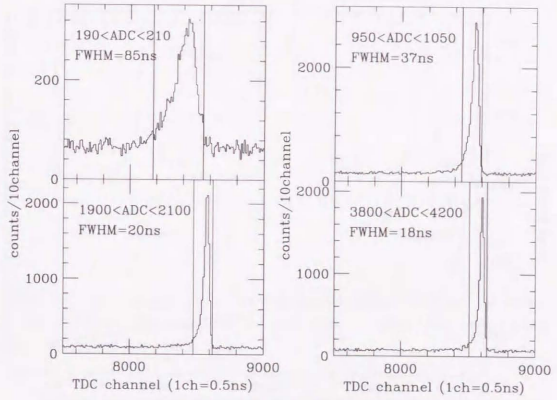

Figure 4.2: *TDC gate of a typical germanium detector for several ADC ranges. One channel of ADC correspond to a γ-ray energy of about 0.6 keV (see Section 4.2). The timing resolution in FWHM is also shown for each TDC spectrum.*

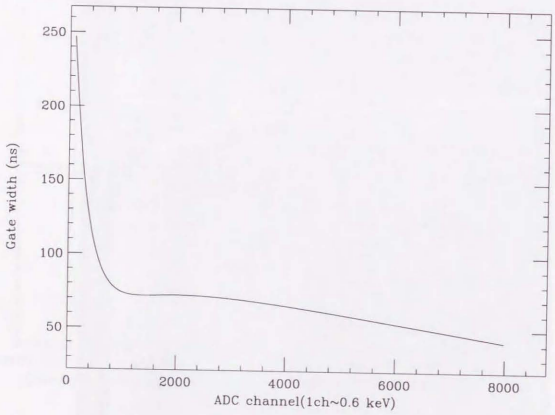

Figure 4.3: *TDC gate width of a typical germanium detector as a function of ADC.*

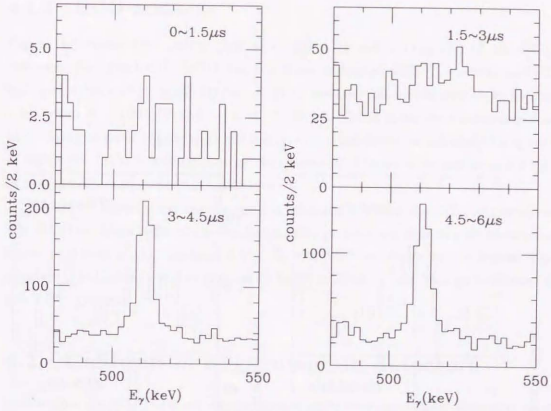

Figure 4.4: *γ-ray energy spectra around the 511 keV (e^+e^-) peak for various pileup conditions. We cannot see the peak when we select those events which have one or more hits within ± 3 μs.*

Utilizing the multihit feature of the TDC (See Section 2.3.6), pileup rejection was applied to germanium hits selected above. A hit was rejected if there was another hit within ± 3 μs in the same germanium detector. γ-ray energy spectra around the 511 keV (e^+e^-) peak for various pileup conditions are shown in Figure 4.4.

4. **Reset veto**

A hit was also rejected if the preamplifier of the germanium detector resets within 15 μs before the hit. As shown in Figure 4.5, we can not see the 511 keV peak if we select events where reset occured within 15 μs.

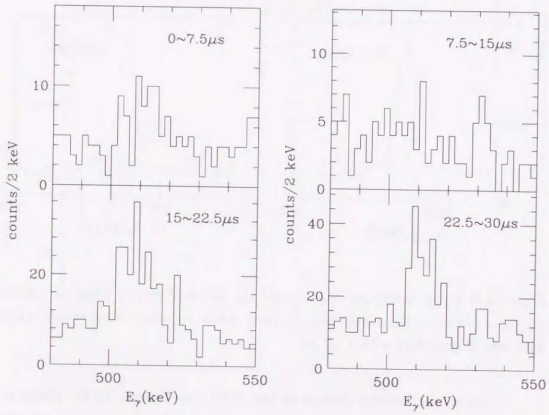

Figure 4.5: *γ-ray energy spectra around the 511 keV (e^+e^-) peak. We cannot see the peak when we select those events which have reset signals within 15 μs.*

4.1.2 BGO counters

Figure 4.6 shows the scatter plot of energy (E) and timing (T) of the BGO counters. Energies for the BGO counters were calibrated with ^{60}Co source and 511 keV γ-rays from e^+e^- annihilation. A BGO counter was considered to be having a hit when $E > 100$ keV and $-4 < T < 100$ ns. Those gates were determined so as to obtain a good suppression efficiency with a moderate accidental killing rate of about 5% [37]. A germanium hit was rejected if there were one or more hits in the corresponding six BGO counters.

Figure 4.7 shows γ-ray energy spectra with and without the BGO suppression. The BGO counters reduced the background in germanium detector by more than factor of 3 over a wide range of $0.5 < E_\gamma < 3$ MeV as shown in the figure. The accidental killing rate was estimated to be $94 \pm 2\%$ from the background level of the TDC spectrum.

4.2 Calibration of germanium detectors

Calibration data for the γ-ray energy measured by the germanium detectors were taken several times during the beamtime in off-beam conditions. We used a standard mixed source which contains ten γ-ray sources covering a wide range of γ-ray energies from 59 keV to 1836 keV (See Table 4.1).

Figure 4.8 shows a plot of ADC versus γ-ray energy of a typical germanium detector for a calibration run. We have used quadratic functions to fit the energies of the calibration peaks. Non-linearity of the calibration curve was typically about 0.1%. Residuals of the fitting are also shown in the figure.

Though the calibration error is as small as $\sim$ 0.3 keV in Figure 4.8, there are two effects which make it worse. One of them is the time dependent drift of the peak position. The size of peak drift was checked by comparing different calibration data and monitored throughout the experiment with the ^{60}Co monitoring system. Figure 4.9 shows the time dependent peak position of the ^{60}Co 1.33 MeV γ-rays measured in the monitoring system and Figure 4.10 shows calibration peaks of ^{88}Y 1.836 MeV γ-rays for a typical germanium detector taken at the beginning and at the end of the beamtime. The peak drift was found to be about 1 $\sim$ 2 keV for those peaks. The γ-ray energy was not corrected for the effect because run by run peak drift observed in the ADC of the monitoring system can be different from that in the ADC of the main DAQ system.

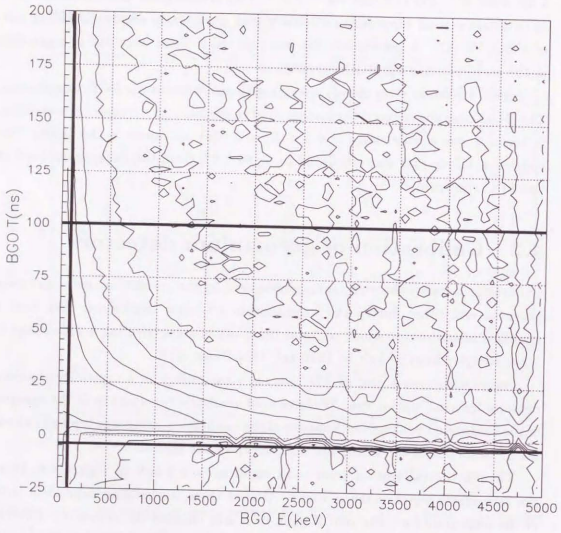

Figure 4.6: *A plot of energy versus timing of the BGO counters. We take the events in the region enclosed by the solid curves as BGO hits.*

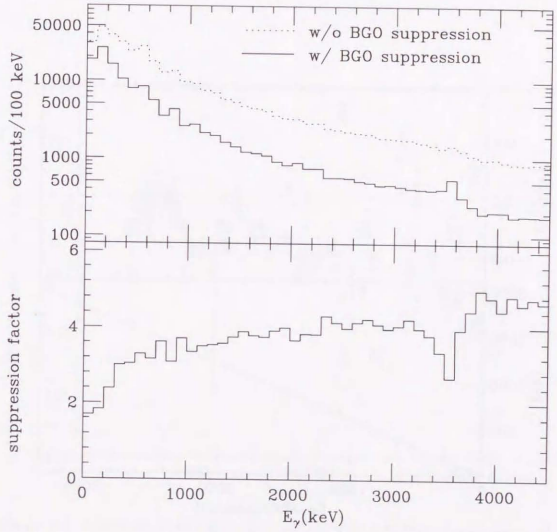

Figure 4.7: *The effect of the BGO suppression; Up: γ-ray energy spectra of germanium detectors for (π^+, K^+) events with and without BGO suppression effect. The solid line and the dotted line are with and without BGO suppression, respectively. Down: suppression factors of the spectra.*

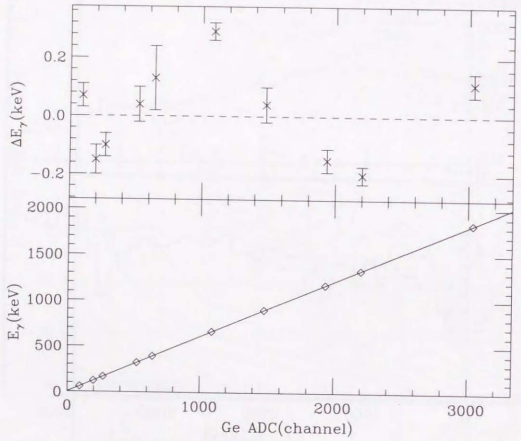

Figure 4.8: *ADC of a typical germanium detector and γ-ray energies. Residuals of the calibration are also shown.*

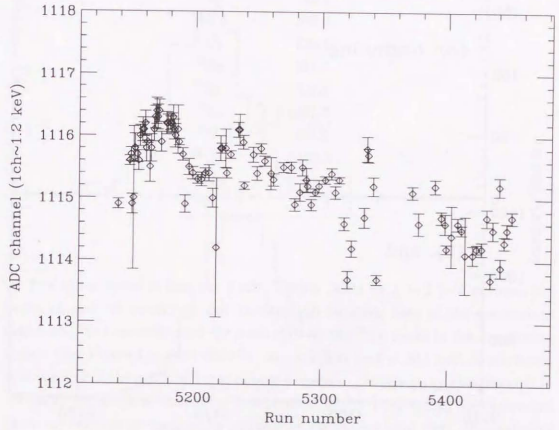

Figure 4.9: *Time drift of the peak position of the ^{60}Co 1.33 MeV γ-rays measured in the monitoring system, for a typical germanium detector. The abscissa is the run number. Typical length of a run is 2 hours.*

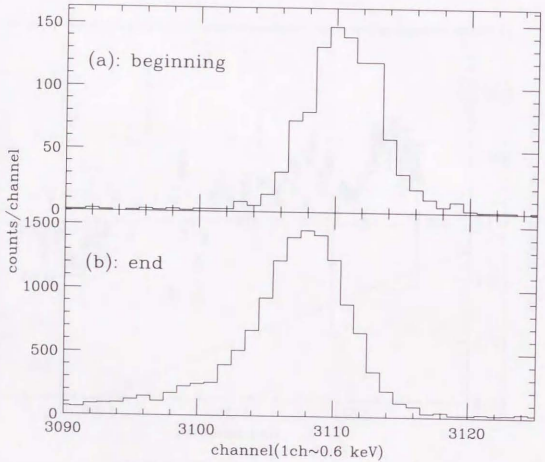

Figure 4.10: *Calibration peaks of ^{88}Y 1.836 MeV γ-rays for a typical germanium detector. Top: at the beggining of the beamtime. Bottom: at the end of the beamtime.*

Table 4.1: *γ-ray sources contained in the mixed source and their γ-ray energies.*

source	γ-ray energy (keV)
^{241}Am	59.5
^{109}Cd	88.0
^{57}Co	122.1
^{139}Ce	165.9
^{51}Cr	320.1
^{113}Sn	391.7
^{85}Sr	514.0
^{137}Cs	661.7
^{88}Y	898.0
^{60}Co	1173.2
^{60}Co	1332.5
^{88}Y	1836.1

The other factor is that the peak position shifts by $1 \sim 2$ keV between the beam on and off conditions due to the high counting rate of the germanium detectors. We have estimated the peak shift by the ^{60}Co peaks in the monitoring system (See Figure 4.11) and the e^+e^- annihilation peak at 511 keV. It was found that the size of the peak shift was almost the same over the γ-ray energies of 0.5–1.3 MeV. We assumed the shift is independent of the γ-ray energy and corrected the γ-ray energies germanium by germanium for the constant shift. We neglected the possible beam intensity dependence and time dependence of the peak shift by taking an average over the whole beamtime.

We have estimated the errors of calibration by using a γ-ray energy spectrum without selecting the true (π^+, K^+) events. By using all the (π^+, K^+) triggers, which were mostly (π^+, p) events, high statistical spectrum was obtained for the same condition as the true $(\pi^+, K^+\gamma)$ events. Figure 4.12 shows the spectrum, in which many peaks of normal nuclear γ-rays, most of which come from secondary reactions in materials around the target (such as aluminium and iron) are seen. Assignments and observed energies of the peaks in Figure 4.12 are tabulated in Table 4.2. From those peaks, the systematic error is estimated to be better than

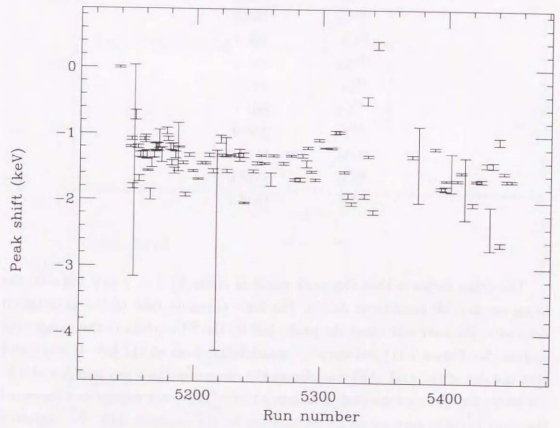

Figure 4.11: *Peak shift between beam on and off for the ^{60}Co 1.33 MeV peak measured in the monitoring system. Peak shift is shown as a function of run number.*

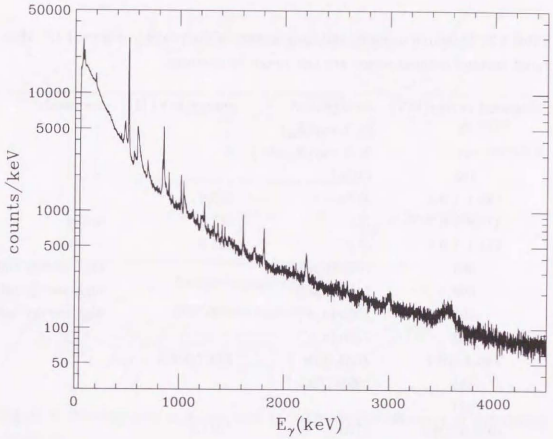

Figure 4.12: *γ-ray energy spectrum without selecting the (π^+, K^+) events.*

0.6 keV for $E_\gamma \lesssim 2$ MeV.

4.3 Efficiencies of germanium detectors

Photo-peak efficiencies of the germanium detectors were calibrated by the same mixed γ-ray source mentioned in Section 4.2. In order to take the target size into account, we put the γ-ray sources at several points in the lithium target volume, as shown in Figure 4.13, after removing the target. The calibration result was compared with a GEANT simulation for each source position, as shown in Figure 4.14. Since the simulations and the calibration data agree well with each others, we used values obtained from the simulation as the photo-peak efficiencies of the germanium detectors. Figure 4.15 shows the photo-peak efficiencies of the germanium detectors calculated from the simulation in the case where the γ-ray sources distribute uniformly in the target volume and absorption of γ-rays in the

Table 4.2: *Measured energies and assignments of the peaks in Figure 4.12. Measured energies without errors are just rough estimations.*

measured energy(keV)	assingnment	energy(keV) [31]	comments
78	Bi X-ray(K_α)		
88	Bi X-ray(K_β etc.)		
198	71Ge?		
440.1 ± 0.3	23Na	440.0	
477.8 ± 0.2	7Li	477.6	broad
511.1 ± 0.1	e^+e^-	511.0	
564	76Ge(n,n')		high-energy tail
596	74Ge(n,n')		high-energy tail
692	72Ge(n,n')		high-energy tail
834	72Ge(n,n')		
846.3 ± 0.1	27Al,56Fe	843.7,846.8	
895	209Bi,72Ge?		
931			
1014.3 ± 0.2	27Al	1014.4	
1022			
1039	70Ge(n,n')		high-energy tail
1130			
1173.3 ± 0.5	60Co	1173.2	
1238.3 ± 0.3	56Fe	1238.3	
1333.4 ± 0.4	60Co	1333.2	
1368.8 ± 0.5	24Mg	1368.6	
1408			
1435			
1609.1 ± 0.5	209Bi	1608.5	
1809.8 ± 0.3	26Mg,56Fe	1808.6,1810.8	broad?
2211.4 ± 0.4	27Al	2211.0	broad
2599	56Fe,209Bi?		
2750	24Mg		broad
3005	27Al?		broad
3550	6Li		broad

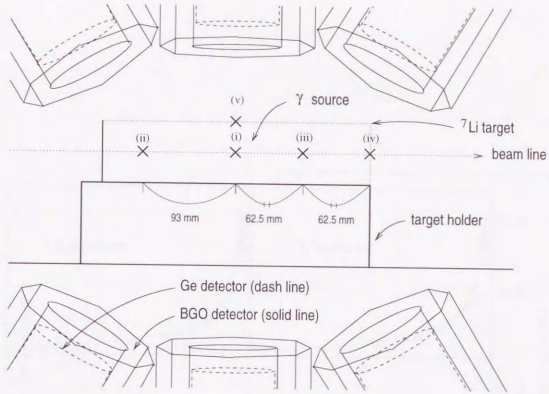

Figure 4.13: *γ-ray source points used to calibrate the efficiency of germanium detectors.*

target is taken into account.

The in-beam livetime was measured by the monitoring system, and found to be $53.8 \pm 0.5\%$ as described in Section 2.3.1. Overall analysis efficiencies were estimated to be $98 \pm 2\%$ and $94 \pm 2\%$ for the TDC cut and the BGO cut, respectively. (See Section 4.1.1 for those cuts) The solid line in Figure 4.15 is the photo-peak efficiency of the germanium detectors including all the effects described above.

4.4 Doppler shift

4.4.1 Doppler shift correction

Since some of the γ-rays from ${}^7_\Lambda$Li are emitted in flight, the measured energies of the γ-rays can be shifted due to the Doppler effect. If we know the velocity of ${}^7_\Lambda$Li and the direction of a γ-ray, Doppler shift can be correccted by the relativistic

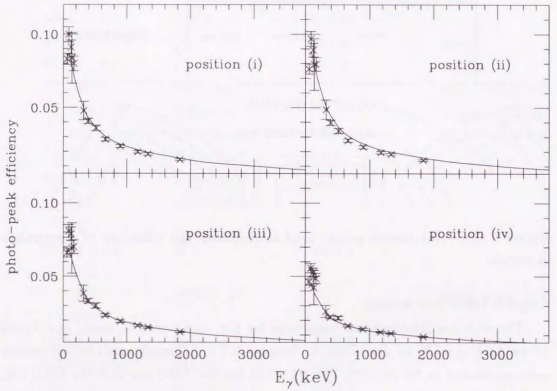

Figure 4.14: *Total efficiency of germanium detectors for each γ-ray source position. The crosses show the measured efficiencies and the solid lines show the simulated efficiencies.*

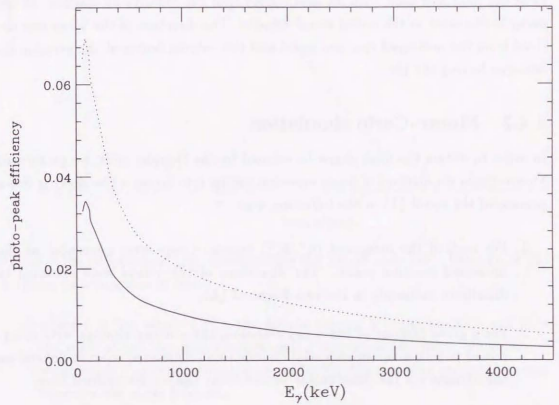

Figure 4.15: *Total efficiency of germanium detectors obtained from the simulation in the case where γ-ray sources distribute uniformly in the target volume. Dotted line: in-beam deadtime and analysis efficiencies are not taken into account. Solid line: those effects are taken into account.*

formula,

$$E_\gamma^{\text{corrected}} = E_\gamma^{\text{measured}} \cdot \gamma(1 - \beta\cos\theta),$$

where $E_\gamma^{\text{corrected}}$ and $E_\gamma^{\text{measured}}$ are the corrected and measured γ-ray energy, respectively, β is the velocity of ${}^{7}_{\Lambda}$Li, γ is defined as $\gamma = 1/\sqrt{1-\beta^2}$, and θ is the angle made by the direction of the γ-ray and the velocity vector of ${}^{7}_{\Lambda}$Li in the laboratory frame. The recoil velocity was calculated from the measured momenta of the pion and kaon with an assumption that the velocity at the time of the decay is the same as the initial recoil velocity. The direction of the γ-ray was derived from the measured reaction point and the volume center of the germanium detector having the hit.

4.4.2 Monte-Carlo simulation

In order to obtain the peak shape broadened by the Doppler shift, we performed Monte-Carlo simulations of γ-ray emission taking into account the slowing down process of the recoil ${}^{7}_{\Lambda}$Li in the following way;

1. For each of the measured (π^+, K^+) events, γ-rays were generated at the measured reaction point. The directions of the γ-rays were assumed to distribute uniformly in the rest frame of ${}^{7}_{\Lambda}$Li.

2. For a given lifetime of the γ-ray emission, the γ-decay timings were determined to follow the exponential distribution. Simulated spectra depend on the lifetime via the distribution of the decay timing determined here.

3. γ-rays were Lorentz boosted with the velocity of ${}^{7}_{\Lambda}$Li at the time of the decay. The velocity at the time of the decay was calculated from the measured recoil momentum and the decay timing using the SRIM code [38].

   Figure 4.16 shows the velocity of ${}^{7}_{\Lambda}$Li as a function of time, calculated by using the stopping power of the SRIM code. We estimated the overall uncertainty of the stopping power of the code to be 5% from the error of the stopping power of various ions in He and Be [39]. It is noted that in non-relativistic approximation, the acceleration is proportional only to the stopping power as;

$$\frac{dv}{dt} = \frac{dv}{dE}\frac{dE}{dx}\frac{dx}{dt} = \frac{1}{mv}\frac{dE}{dx}v = \frac{1}{m}\frac{dE}{dx},$$

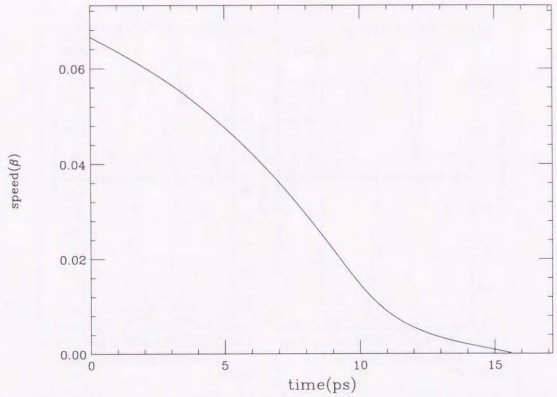

Figure 4.16: *Stopping of ${}^{7}_{\Lambda}$Li calculated by the SRIM code [38]. Velocity of ${}^{7}_{\Lambda}$Li is shown as a function of time.*

   where v is the velocity, E is the kinetic energy, x is the position and m is the mass of the stopping particle, and t represents the time. Therefore, if we increase the overall stopping power by 5%, the stopping process becomes faster by the same fraction.

4. If a γ-ray hits the effective volume of a germanium detector, the energy of the γ-ray was filled into a histogram. The effective volume of a germanium detector was taken to be a sphere of a 30 mm radius in the simulation program. The simulation result depends little on how to take the effective voulume of the germanium detector. Doppler shift correction for the simulated data was also performed in the same way. We took into account the position resolution of the vertex point in the simulation of the Doppler shift correction.

Since photons are massless, the Doppler factor, z, is independent of the γ-ray energy. Figure 4.17 shows the doppler factor distribution obtained by the

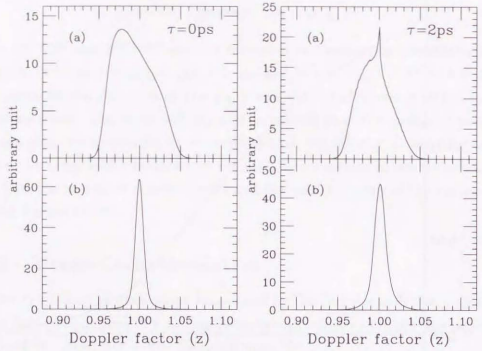

Figure 4.17: *Distribution of Doppler factor for lifetimes of $\tau = 0, 2$ ps obtained by the Monte Carlo simulation; (a): without Doppler shift correction, (b): with Doppler correction.*

simulation for various lifetimes. When the assumed lifetime is zero, the peak is fully broadened without Doppler shift correction, while it is much shaper with Doppler shift correction. For longer lifetimes, sharp peak appears in the Doppler uncorrected spectra due to γ-ray emission after the stopping of $^{7}_{4}$Li, but the effect of Doppler shift correction becomes worse. It is noted that the shape of the peak is not left-right symmetric, because there are more germanium detectors in the upstream side than the downstream side (see Section 2.3.5). For finite lifetimes, this effect makes the peak positions in Doppler shift corrected spectra higher than the real γ-ray energy.

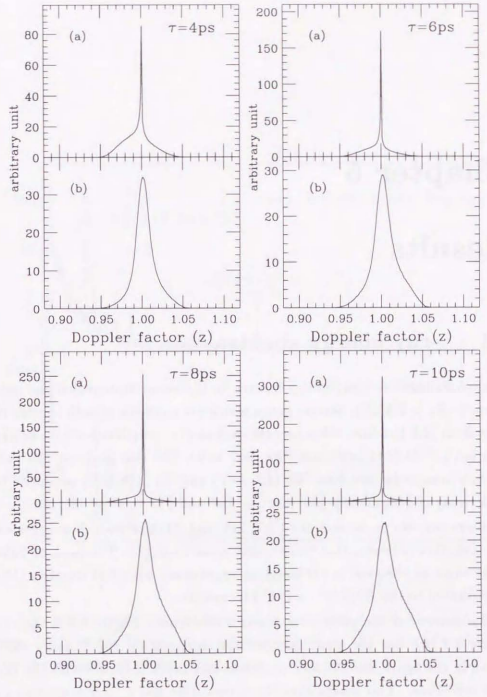

Figure 4.17 (continued): *Distribution of Doppler factor for lifetimes of $\tau = 4, 6, 8, 10$ ps obtained by the Monte Carlo simulation; (a): without shift Doppler correction, (b): with Doppler correction.*

Chapter 5

Results

5.1 γ-ray energy spectra

Figure 5.1 shows the γ-ray energy spectra for the bound state region and unbound region ($-B_\Lambda > 2$ MeV). Several peaks which are common to both spectra do not come from ${}^{7}_{\Lambda}$Li, but from other sources such as e^+e^- annihilation (511 keV), ^{74}Ge (596 keV), ^{27}Al (844 keV) and ^{56}Fe (847 keV). The two peaks at 429 keV and 478 keV seen in (a) are from ^{7}Be (429 keV) and ^{7}Li (478 keV) produced by the weak decay of ${}^{7}_{\Lambda}$Li, namely ${}^{7}_{\Lambda}\mathrm{Li} \to \pi^- + {}^{7}\mathrm{Be}^{\bullet}$ and ${}^{7}_{\Lambda}\mathrm{Li} \to \pi^0 + {}^{7}\mathrm{Li}^{\bullet}$.

There are two peaks at around 690 keV and 2050 keV which are seen only in (a). This fact indicates that those peaks come from ${}^{7}_{\Lambda}$Li. The peak at 2050 keV is the same as observed in the previous experiment with NaI counters [15], and is attributed to the $E2(5/2^+ \to 1/2^+)$ transition.

Assignment of the other peak needs a discussion. Figure 5.2 is the same as Figure 5.1 (a), but the γ-ray energies are corrected for the Doppler shift. As shown in the figure, the 690 keV peak becomes much narrower with the Doppler shift correction. This means that the γ-transition has a large transition rate of more than $(\sim 3\ \mathrm{ps})^{-1}$ (see Figure 4.17). If the transition is an $E2$ transition, the reduced transition rate must be larger than 1700 $e^2\mathrm{fm}^4$, which is too large for such a light (hyper-)nuclei[1]. We don't think about a possibility of an $E1$ transition, because no negative parity states are expected in the bound state region. Therefore, we conclude that the transition has a multipolarity of $M1$.

In the bound state region of ${}^{7}_{\Lambda}$Li (see Figure 1.3), there are five candidates for

[1] If we use the Weisskopf unit, this corresponds to 2.1×10^3 W.u.

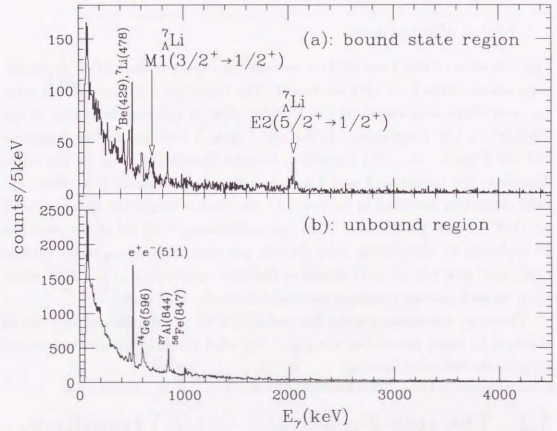

Figure 5.1: *γ-ray energy spectra measured in coincidence with the ${}^{7}\mathrm{Li}(\pi^+, K^+)$ reaction. (a) is for the bound state region and (b) is for the unbound region. See text for the assignment of the peaks.*

an $M1$ transition[2]:

1. Spin-flip $3/2^+ \rightarrow 1/2^+$ transition.
2. Spin-flip $7/2^+ \rightarrow 5/2^+$ transition.
3. $1/2^+(T=1) \rightarrow 1/2^+$ transition.
4. $1/2^+(T=1) \rightarrow 3/2^+$ transition.
5. $5/2^+ \rightarrow 3/2^+$ transition.

The transitions 3 and 4 are unlikely because the expected energies of the transitions are too large ($\sim$ 3 MeV or larger). The transition 5 is also unlikely since the peak shape determined by the Doppler effect is different from that of the $E2(5/2^+ \rightarrow 1/2^+)$ transition. If the initial state is common to this transition and the $E2(5/2^+ \rightarrow 1/2^+)$ transition, Doppler broadening must be the same. Therefore, the transition 1 and 2 are the only possible candidates. From the yield estimation described in Section 5.2.2, the peak is attributed to the spin-flip $M1(3/2^+ \rightarrow 1/2^+)$ transition. With this assignment, the yield of the peak can be explained by considering γ-ray cascade processes from upper states such as $5/2^+$, $7/2^+$ and $1/2^+(T=1)$ as well as the direct production of the $3/2^+$ state, while no such cascade processes are available for the $7/2^+$ state.

Those two transitions are the first well-identified γ-transitions of hypernuclei observed by using germanium detectors. Detailed descriptions about them are given in the following sections.

5.2 The spin-flip M1$(3/2^+ \rightarrow 1/2^+)$ transition.

5.2.1 γ-ray energy

Figure 5.3 shows γ-ray energy spectra around the $M1$ peak with and without the Doppler shift correction. To obtain the energy of the transition, the Doppler corrected spectrum was fitted to a gaussian with a linear background. The result of the fitting is shown in the figure. From the fitting, the position of the peak was obtained to be 691.9 ± 0.6 keV, where the error is statistical. The width

[2]In the present discussion, we are assuming that the $3/2^+$ ($7/2^+$) state is the upper part of the ground (first excited) state doublet. This assumption can be justified in several ways as described in Appendix B.

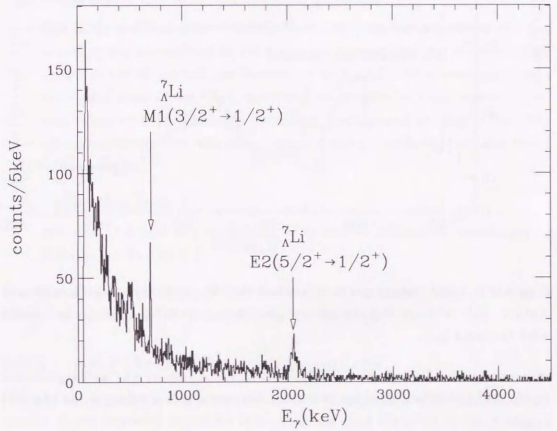

Figure 5.2: *γ-ray energy spectrum for the bound state region after Doppler shift correction. See text for the assignment of the peaks.*

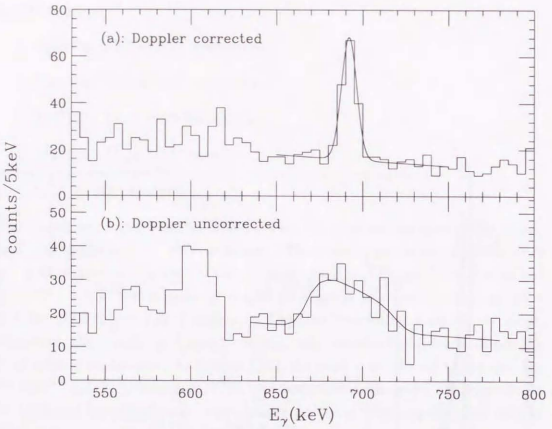

Figure 5.3: *γ-ray energy spectrum around the M1 peak; (a): with Doppler correction. (b): without Doppler correction. The results of the fittings are shown with the solid lines.*

obtained by the fitting was 4.5 ± 0.5 keV in r.m.s., which was well reproduced by the Monte Carlo simulation (4.4 keV). The yield was obtained to be 119 ± 14 counts.

Corrections and systematic errors of the γ-ray energy

1. **Correction due to finite lifetime**

   According to Monte-Carlo simulations, the position of the peak obtained in this way is 0.2 keV higher than the real γ-ray energy. This is because of the finite lifetime of the $3/2^+$ state, which was taken to be 0.5 ps from the calculated $B(M1)$ values in Refs. [30, 2] (see Section 4.4.2).

   If we further incorporate the γ-ray cascade process from upper states with long lifetimes, this correction can be larger. We estimated the effect by assuming that 20% of the events come from such states as $5/2^+$, of which lifetime is obtained to be 5.8 ps in Section 5.3.2. With this assumption, the position of the peak was 0.4 keV higher than the true γ-ray energy in the simulation.

   Therefore, the obtained γ-ray energy was reduced by 0.2 keV with a systematic error of ± 0.2 keV.

2. **Uncertainty of the z-vertex center position**

   The center position of the z-vertex distribution has an uncertainty of 5 mm including the uncertainty of the target position (3 mm) in the coordinate system of the Hyperball (see Section 3.7 and 2.2.3). This corresponds to a systematic error of ± 0.8 keV, according to Monte-Carlo simulations. Random errors of z-vertex cancel by taking average and are negligible. The systematic errors from the offsets of the x and y coordinates are also found to be negligible.

3. **Calibration error**

   We take ± 0.5 keV as a systematic error due to calibration uncertainty as discussed in Section 4.2.

Considering the corrections and systematic errors above, the energy of the transition is obtained to be $691.7 \pm 0.6(\text{stat.}) \pm 1.0(\text{syst.})$ keV.

5.2.2 γ-ray yield and peak assignment

We used the Doppler shift uncorrected spectrum to obtain the yield of the peak, instead of the corrected one. This is because the yield obtained by the fitting of Doppler shift corrected spectrum is expected to be smaller than the actual value due to the event loss at the small horizontal scattering angles. Doppler shift correction does not work properly for such events, because of the bad z-vertex resolution.

The Doppler shift uncorrected spectrum was fitted to a simulated spectrum with a linear background. In the simulation, lifetime of the $3/2^+$ state was taken to be 0.5 ps, and the energy of the γ-ray was fixed to be 691.7 keV. The fitting result is shown in Figure 5.3. It is shown that the spectrum can be well reproduced by the Monte Carlo simulation. The obtained yield was 128 ± 17 counts, which is larger than the value obtained from the Doppler corrected spectrum as expected.

According to the simulations, the yield difference can be explained by the effect described above.

This yield can not be explained by the direct production process of the $3/2^+$ state, since the state have to be produced by the spin-flip amplitude which is known to be much smaller than the non spin-flip amplitude in the (π^+, K^+) reaction [32]. According to the calculation by Hiyama *et al.*, the reaction cross section of the $3/2^+$ state is about 10% of the $1/2^+$ state [30]. Taking the produced number of the $1/2^+$ state to be 2.98×10^4 from Table 3.1, and believing the ratio of the theoretically calculated production cross section, the yield of the transition from the direct production process is estimated to be 39 counts using the efficiency of the germanium detectors obtained in Section 4.3. This is more than three times smaller than the observed counts, which indicates that the $3/2^+$ state is mainly populated by the γ-ray cascade processes. This situation is similar for the $7/2^+$ state, but there are no γ-ray cascade processes to populate the $7/2^+$ state. Therefore, it is concluded that the observed transition is the $M1(3/2^+ \rightarrow 1/2^+)$ transition.

If the γ-ray cascades are really the dominant processes to populate the $3/2^+$ state, some of the feeding γ-rays might be observed in the experiment. This possibility is discussed in Section 5.4.3.

5.3 The $E2(5/2^+ \rightarrow 1/2^+)$ transition

Figure 5.4 is a magnification of the 2050 keV region, shown in Figure 5.1 (a). The peak has two components, namely the narrower part and the broader part which is due to the Doppler shift.

5.3.1 γ-ray energy

To obtain the energy of the γ-rays, the peak is fitted with two gaussians (one for the narrower part and the other for the broader part) plus a linear background. The fitting result is 2050.1 ± 0.4 keV, where the error is statistical. The systematic error due to the calibration uncertainty is estimated to be ± 0.6 keV. Selection of fitting function for the broader peak gives further systematic error of 0.3 keV. Therefore the γ-ray energy is obtained to be $2050.1 \pm 0.4(\text{stat.}) \pm 0.7(\text{syst.})$ keV. Considering a small recoil energy (0.3 keV) of ${}^7_4\text{Li}$, the excitation energy of the $5/2^+$ state is resulted in $2050.4 \pm 0.4(\text{stat.}) \pm 0.7(\text{syst.})$ keV. This value is consistent

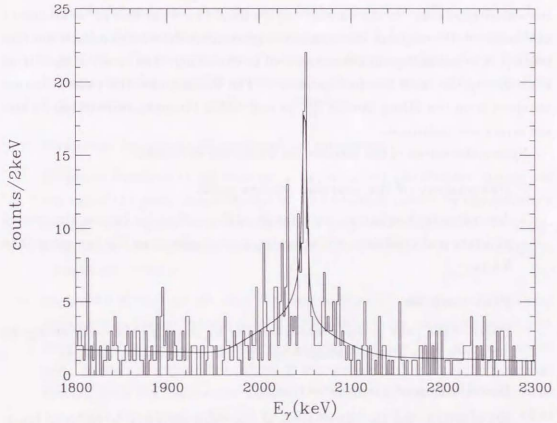

Figure 5.4: *γ-ray energy spectrum around the E2 peak. The result of the fitting to the simulated spectrum is shown with the solid line.*

with the result of the old experiment with NaI counters (2034 ± 23 keV), and the precision of the present result is more than one order of magnitude better than that. Indeed, this energy precision is a new world record of hypernuclear experiments.

5.3.2 Lifetime analysis

Lifetime of the $5/2^+$ state was derived from the shape of the peak by fitting the simulated spectrum. In the simulation, we fixed the γ-ray energy to be 2050.1 keV and took the response function of the germanium detectors into account (see below). A linear background was assumed in the fitting. The result of the fitting is shown by the solid line in Figure 5.4. The lifetime and the yield of γ-rays obtained from the fitting are $5.8\ ^{+0.9}_{-0.7}$ ps and 192 ± 17counts, respectively, where the errors are statistical.

Systematic errors of the lifetime are estimated as follows.

1. **Uncertainty of the reaction vertex point**

   According to simulations, uncertainty of the z-offset for the reaction vertex of 5 mm and resolution of the vertex do not affect the lifetime more than 0.1 ps.

2. **Peak position**

   Effect of the peak position was estimated by changing the γ-ray energy by ± 0.4 keV. The lifetime changed by ± 0.1 ps as the energy changes.

3. **Distribution of γ-ray direction**

   We assumed that the distribution of the γ-ray direction is uniform, but it may not be the case since the spins of produced ${}^{7}_{\Lambda}$Li are expected to be aligned in the normal direction of the reaction plane. As an extreme, we simulated a case where all the $5/2^+$ states are aligned to $|j_z| = 5/2$. In this simulation, the obtained lifetime is 0.4 ps longer than the uniform case. Thus the systematic error due to this is estimated to be ± 0.4 ps.

4. **Recoil momentum**

   As explained in Section 3.8.1, there is some uncertainty in the absolute scale of the pion and kaon momenta. This uncertainty cancels largely in the recoil momentum, as we take the differnce of the two momenta. As a result, the uncertainty is about 1 MeV/c, which is only 0.3% of a typical recoil momentum and is negligible in the lifetime analysis.

   The random error of recoil momentum is also negligible, since they cancel each others by taking average.

5. **Stopping power**

   As explained in Section 4.4.2, we estimated the error of the stopping power of the SRIM code and thus the error of the lifetime is $\pm 5\%$ (± 0.3 ps). It is noted that the uncertainty of the stopping power is larger at velocities lower than $0.01c$. However, this hardly increase the uncertainty of the lifetime because the velocity of ${}^{7}_{\Lambda}$Li at the time of the γ-ray emission is larger than $0.01c$ in most cases.

6. **Response functions of germanium detectors**

   Response functions of germanium detectors affect the lifetime mainly via the tail of the peak. Since the tail of the peak is produced by the radiation damage of the germanium detectors, it is very much different at the beginning and at the end of the beamtime, as shown in Figure 4.10 for a typical germanium detector.

   Figure 5.5 shows the response function used in the simulation. This was derived from the calibration data of 1.836 MeV γ-rays, extrapolated to 2.05 MeV and averaged over all the germanium detectors and the calibration runs through the whole beamtime. When we used other response functions derived from the calibration data at the beginning and at the end of the beamtime, the lifetime changed by -0.4 ps and $+0.3$ ps, respectively. Thus we take $^{+0.3}_{-0.4}$ ps for the systematic error.

7. **Reaction vertex cut**

   To estimate the effect of the z-vertex cut (see Section 3.7), we studied the cases where the vertex cuts were |(z-vertex)| <100, 125 (actual target size) and 200 mm. With those conditions, the lifetime changes no more than 0.1 ps. We also performed a simulation in which we assumed the vertex point distributes uniformly in the target instead of using that of the real events. The lifetime has not changed with this simulation. Thus the systematic error due to the reaction vertex cut was found to be negligible.

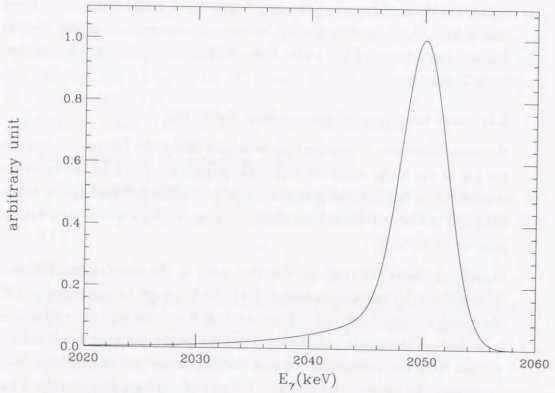

Figure 5.5: *Response function used in the Monte-Carlo simulation.*

8. **Horizontal reaction angle cut**

   The effect of horizontal scattering angle cut described in Section 3.7 was studied by changing the cut condition to $|\theta_{\rm horizontal}| < 5$, 15 and 20 mrad. The lifetime changed by 0.1 ps as the cut changes. This is much smaller than the statistical error and thus we neglected the systematic uncertainty due to the horizontal scattering angle cut.

9. **B_Λ gate**

   In order to study the B_Λ gate dependence of the lifetime, we studied the cases where the upper bound of the $-B_\Lambda$ gate is 0, 1, 3 and 4 MeV instead of 2 MeV (see Section 3.8.2). The lifetime changed no more than 0.1 ps with those bounds. Therefore we neglected the systematic error due to the B_Λ gate.

10. **Fitting region**

    The fitting was performed in the region of $1800 < E_\gamma < 2300$ keV. Selection of fitting region might affect the lifetime via the estimation of the background level. In order to study this effect, we changed the fitting region to $1825 < E_\gamma < 2275$ keV and $1850 < E_\gamma < 2250$ keV[3]. The lifetime became shorter by 0.1 ps as the fitting region becomes narrower to ± 200 keV of the peak. Thus we neglected the systematic error due to the selection of the fitting region.

11. **Effect of the $7/2^+$ state**

    γ-ray cascade process from upper states can make the lifetime seem longer because of the lifetime of the upper state. In the case of the $5/2^+$ state in ${}^{7}_{\Lambda}$Li, the $7/2^+$ state is the only candidate for the parent state of the γ-ray cascade. We estimated the effect of the cascade process from initial $7/2^+$ state by assuming the followings;

    (a) Production cross section of the $7/2^+$ state was taken to be 6.5% of the $5/2^+$ state according to Ref. [30].

[3]The fitting region must be wide enough compared to the Doppler width of the peak (± 120 keV at maximum) to obtain a proper backbround level. Thus, we should avoid to use fitting regions narrower than ± 200 keV.

(b) Excitation energy of the $7/2^+$ state was assumed to be 2.48 MeV according to Millener's phenomenological calculation [26] which reproduces the excitation energies of the $3/2^+$ and $5/2^+$ states obtained in the present experiment.

(c) Lifetime of the $7/2^+$ state was calculated to be 2.0 ps by using the $B(E2; 7/2^+ \rightarrow 3/2^+)$ and $B(M1; 7/2^+ \rightarrow 5/2^+)$ values of Hiyama *et al.* [30]. Branching ratio of the $7/2^+ \rightarrow 5/2^+$ transition was estimated to be 0.85 from the same calculation.

In the simulation where the effect of the $7/2^+$ state was taken into account using those assumptions, the lifetime of the $5/2^+$ state became shorter by 0.1 ps. Thus we neglected the systematic error from this effect.

In total, the systematic error is estimated as ± 0.7 ps by summing up the errors estimated above in quadrature. Thus the lifetime is obtained to be $5.8\,^{+0.9}_{-0.7} \pm 0.7$ ps.

5.4 Other transitions

5.4.1 The $5/2^+ \rightarrow 3/2^+$ transition

Since the excitation energy of the $5/2^+$ and $3/2^+$ states are known to be 2050.4 keV and 691.7 keV, a peak for the $5/2^+ \rightarrow 3/2^+$ transition should be observed at 1358.6 keV[4] if the yield is large enough. In the experiment, however, we did not observe the peak as shown in Figure 5.6. We set an upper limit of the branching ratio of the transition to be 4.3% at 68% confidence level.

In the weak coupling limit, the transition is a pure $E2$ transition, and the branching ratio of the $5/2^+ \rightarrow 3/2^+$ transition is estimated to be

$$\frac{BR(5/2^+ \rightarrow 3/2^+)}{BR(5/2^+ \rightarrow 1/2^+)} = \frac{2}{7}\left(\frac{\Delta E(5/2^+, 3/2^+)}{\Delta E(5/2^+, 1/2^+)}\right)^5 = 0.037.$$

By using the $B(E2; 5/2^+ \rightarrow 3/2^+)$ value of Hiyama *et al.* [30], the branching ratio is calculated to be 3.8%. Those calculations are consistent with the present upper limit. This indicates that the $M1$ component of the transition is small, as expected from the weak coupling assumption.

[4]This value includes a small correction of -0.1 keV for recoil of ${}^7_\Lambda$Li.

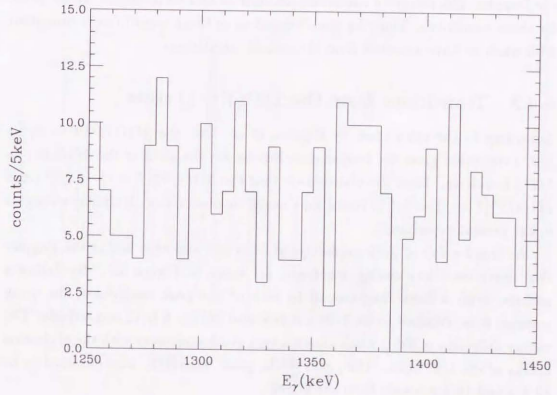

Figure 5.6: *γ-ray energy spectrum around 1350 keV. There is no peak at 1359 keV, being consistent with what is expected from the weak coupling assumption.*

5.4.2 Transitions from the $7/2^+$ state

We did not find peaks for the transitions from the $7/2^+$ state. If we use the same assumption as in the Section 5.3.2 for the excitation energy of the $7/2^+$ state and the transition rates of the $7/2^+ \to 3/2^+$ and $7/2^+ \to 5/2^+$ transitions, we would expect two peaks of 2 and 29 counts at 1.79 MeV and 0.43 MeV, respectively. On the other hand, the background levels at these energies are respectively 6 and 35 counts per 5 keV, and the expected widths are 13 and 4.2 keV (r.m.s.) in the Doppler shift corrected spectrum, we need 33 and 43 counts to see 3σ peaks for those transitions. Thus the non-observation of those transitions is consistent with what we have expected from theoretical calculations.

5.4.3 Transitions from the $1/2^+(T=1)$ state

According to the calculation by Hiyama *et al.* [30], the $M1(1/2^+(T=1) \to 3/2^+)$ transition gives the largest contribution for the yield of the $M1(3/2^+ \to 1/2^+)$ transition. Their calculation says that the $M1(1/2^+(T=1) \to 3/2^+)$ and $M1(1/2^+(T=1) \to 1/2^+)$ transitions might be observed with similar strengths in the present experiment.

We found a pair of peak candidates at 3180 keV and 3880 keV in the Doppler shift corrected γ-ray energy spectrum, as shown in Figure 5.7. By fitting a gaussian with a linear background to each of the peak candidates, the γ-ray energies were obtained to be 3182 ± 3 keV and 3877 ± 6 keV, respectively. The energy difference of 695 ± 7 keV shows a very good agreement with the excitation energy of the $3/2^+$ state. The yields of the peak candidates were obtained to be 18 ± 5 and 16 ± 6 counts from the fitting.

We further tried another fit by assuming several constraints as;

1. The energy difference of the two peaks was taken to be 691.3 keV[5] from the excitation energy of the $3/2^+$ state.

2. The widths of gaussians for the peaks were fixed to the Doppler width after the Doppler shift correction (15 and 18 keV in r.m.s., respectively) obtained in the Monte-Carlo simulation. It is noted that the expected lifetime of the $1/2^+$ state is an order of 0.1 fs, and thus the effect of Doppler shift attenuation is negligible.

[5]Recoil energy of ${}^{7}_{\Lambda}$Li was taken into account.

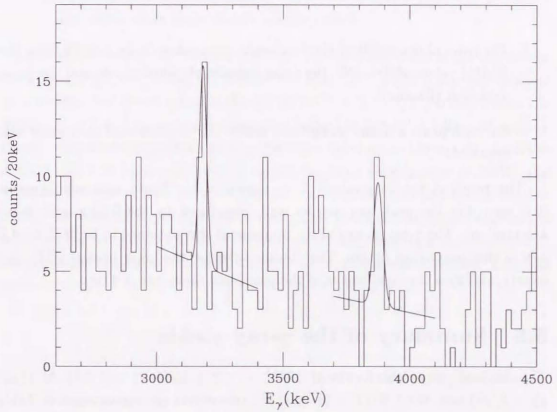

Figure 5.7: *γ-ray energy spectrum of high energy region with Doppler correction. There is a pair of peak candidates at 3182 ± 3 keV and 3877 ± 6 keV. The result of the constrained fit described in the text is shown with solid curves.*

Table 5.1: *Summary table of the obtained yields of the γ-rays.*

γ-transition	E_γ(MeV)	γ-ray yield
$M1(3/2^+ \to 1/2^+)$	0.69	128 ± 17
$E2(5/2^+ \to 1/2^+)$	2.05	192 ± 17
$M1(1/2^+(T=1) \to 3/2^+)$	3.18	19.7 ± 4.6
$M1(1/2^+(T=1) \to 1/2^+)$	3.88	14.8 ± 3.5

3. The ratio of the yields of the two peaks were taken to be 1 : 0.75 from the $B(M1)$ values of Ref. [30], the γ-ray energies obtained above, and the γ-ray detection efficiency.

4. For each peak, a linear background which is independent of each other was assumed.

The result of the constrained fit is shown in the figure with solid curves. It is seen that the peak pair can be well reproduced by the fitting with those assumptions. The γ-ray energy of the upper peak was obtained to be 3875.2 ± 4.0 keV in the constrained fitting. The obtained yield of the lower peak is 19.7 ± 4.6 counts, and thus the significance of the pair peak candidate is 4.3σ.

5.5 Summary of the γ-ray yields

The obtained γ-ray yields for the $M1(3/2^+ \to 1/2^+)$, $E2(5/2^+ \to 1/2^+)$, $M1(1/2^+(T = 1) \to 3/2^+)$ and $M1(1/2^+(T = 1) \to 1/2^+)$ transitions are summarized in Table 5.1. The yields of the last two transitions from the $1/2^+(T = 1)$ state are taken to the value obtained for the pair peak candidates described in Section 5.4.3

The yield of the $E2(5/2^+ \to 1/2^+)$ is consistent with the value estimated to be 192 counts from the number of $5/2^+$ state produced by the (π^+, K^+) reaction (3.36×10^4, see Table 3.1), the branching ratio of the $5/2^+ \to 1/2^+$ transition (93.6%, see Section 6.2) and the detector efficiency (0.61%, see Section 4.3).

From the yield of the $1/2^+(T = 1)$ state in Table 3.1, the expected yield of the $M1(1/2^+(T = 1) \to 3/2^+)$ and $M1(1/2^+(T = 1) \to 1/2^+)$ transitions are respectively 40 and 30 counts, which are about two times larger than the obtained yields for the peak candidates. There are two possible explanations for this yield discrepancy;

1. The real production yield of the $1/2^+(T = 1)$ state is smaller than that in Table 3.1. In this case, the remaining yield is ascribed to other states, such as the second $3/2^+$ state[6].

2. The particle decay threshold for ${}^5_\Lambda\mathrm{He} + d$ at 3.94 ± 0.04 MeV [36] is actually located below the $1/2^+(T = 1)$ state at 3.88 MeV. In this case, the partial decay rates of the particle decay and the γ-decays can be the same order, because the particle decay from $T = 1$ states are suppressed due to isospin conservation while the γ-decays are very fast[7].

Anyway, if we take the values in Table 5.1 for the γ-ray yields of the transitions from the $1/2^+(T = 1)$ state, the yield of the $M1(3/2^+ \to 1/2^+)$ can be explained consistently. The contribution of the $M1(1/2^+(T = 1) \to 3/2^+)$ transition for the $M1(3/2^+ \to 1/2^+)$ transition is calculated to be $(19.7/0.41) \times 1.21 = 58$ counts. Combined with the contributions from the direct production (39 counts), from the $E2(5/2^+ \to 3/2^+)$ state (15 counts, taking the branching ratio to be 3.8%) and from the $7/2^+$ state (4 counts, for the same assumption as described in Section 5.3.2), the calculated yield is 116 counts. This is consistent with the observed value within one statistical error. This fact strongly supports the existence of the peaks for the transitions from the $1/2^+(T = 1)$ state at 3.18 MeV and 3.88 MeV.

[6]The main component of this state is ${}^6\mathrm{Li}(2^+, 4310\ \mathrm{keV}) \otimes s_\Lambda$.

[7]The expected transition rates are an order of $(0.1\ \mathrm{fs})^{-1}$ from the $B(M1)$ values in Ref. [30]

Chapter 6

Discussion

6.1 The ΛN spin-spin interaction

The excitation energy of the $3/2^+$ was obtained to be $691.7 \pm 0.6 \pm 1.0$ keV. If we use the simplest formula (1.1), the Δ parameter is derived to be 0.46 MeV. More realistically, we have to estimate the effects of spin-orbit and tensor interactions. We used S_Λ, S_N and T parameters of various potential models in Table 1.1. The results are $\Delta = 0.48 \sim 0.50$ MeV as shown in Table 6.1 for the formula (1.3). The effects of those interactions are 20 keV at most in these potential models.

The obtained value is consistent with $\Delta \sim 0.5$ MeV estimated from the four-body hypernuclear data [3]. In a recent four-body (α-n-p-Λ) cluster model calculation by Hiyama *et al.* [40], the present result is also consistent with the strength of the spin-spin estimated from the four-body hypernuclear data. They modified the strength of the spin-spin interaction of Nijmegen model F potential (NF) [7] to reproduce the 0^+ and 1^+ splitting of four-body hypernuclei and obtained 650 keV for the excitation energy of the $3/2^+$ state, without effects of the spin-orbit interactions. Thus the strength of the ΛN spin-spin interaction is experimentally

Table 6.1: Δ *parameters obtained by fixing the other paramters to the original values of various potentials. See caption of Table 1.1 for the names of the potential models.*

	Millener	Fetisov	ND	NF	NSC89	NSC97f	JA	JB
Δ(keV)	489	484	490	494	494	498	484	484

established. This gives a stringent constraint to the ΛN potential models.

As for the ${}^{10}_{\Lambda}$B experiment which is the base for the Fetisov's estimation ($\Delta =$ 0.3 MeV) [4], contributions of other interactions are doubted for the reason of the missing γ-ray if it is truly missing. We would like to repeat the ${}^{10}_{\Lambda}$B experiment to check their result with the Hyperball, being a more efficient germanium detector system.

6.2 $B(E2)$ and hypernuclear size

The lifetime of the $5/2^+$ state was obtained to be $5.8^{+0.9}_{-0.7} \pm 0.7$ ps. To convert this lifetime into the $B(E2; 5/2^+ \rightarrow 1/2^+)$ value using Equation 1.5, we have to know the branching ratio of the $E2(5/2^+ \rightarrow 1/2^+)$ transition. There are two other possible decays, namely, the $5/2^+ \rightarrow 3/2^+$ transition and the weak decay.

We take 3.8% from Ref. [30] as the branching ratio of the $5/2^+ \rightarrow 3/2^+$ transition. Branching ratio of the latter process is estimated to be 2.6%, by assuming the partial decay rate of the weak decay to be $(230 \text{ ps})^{-1}$ from the data of $A = 4, 5, 11, 12$ hypernuclei [41, 42, 43, 44]. Thus the branching ratio of the $E2(5/2^+ \rightarrow 1/2^+)$ transition is obtained as 93.6%.

Now the $B(E2; 5/2^+ \rightarrow 1/2^+)$ can be calculated using Equation 1.5, and the result is obtained to be $3.6 \pm 0.5^{+0.5}_{-0.4}$ $e^2\text{fm}^4$. The present result is significantly smaller than the value of $B(E2) = 8.6 \pm 0.7$ $e^2\text{fm}^4$ expected when we don't take into account the shrinking effect. Therefore, we conclude that the shrinking effect is observed and that the glue-like role is verified experimentally. The present result corresponds to a nuclear-size shrinkage of $19 \pm 4\%$ using Equation 1.4.

Table 6.2 shows the results of various calculations for the size of each state of ${}^{7}_{\Lambda}$Li and ^{6}Li and for the $B(E2)$ value of each transition. The shell model calculation does not take into account the shrinking effect, and thus gives the same result ($B(E2) = 8.6$ $e^2\text{fm}^4$) as our estimation above. The cluster model calculations show better agreement with the present result, but the shrinking effect obtained in the present experiment is smaller than their calculations.

Table 6.2: *Sizes of the various states of* ^{6}Li *and* $^7_\Lambda$Li *calculated by (a): Hiyama et al. (*$\alpha(^5_\Lambda$He*)-p-n cluster model) [29], and (b): Motoba et al. (*α*-d-*Λ *cluster model) [28]. Sizes are represented by the root-mean-square distance between* α *and d(p-n). Reduced transition probabilities, B(E2), are also shown. Results from (c): a shell model calculation (without shrinkage effect) by Dalitz and Gal [2] and (d): experiment [31] are cited for reference.*

		(a) $\alpha(^5_\Lambda$He$)$-p-n cluster model	(b) α-d cluster model	(c) shell model	(d) exp.
^{6}Li	B(E2)[e^2fm^4]	9.96	6.6	11	10.9±0.9
	$R_{\alpha\text{-}d}(1^+)$[fm]	3.85	3.80		
	$R_{\alpha\text{-}d}(3^+)$[fm]	—	3.66		
$^7_\Lambda$Li	B(E2)[e^2fm^4]	2.42	2.5	8.6	
	$R_{\alpha\text{-}d}(1/2^+)$[fm]	2.94	3.13		
	$R_{\alpha\text{-}d}(5/2^+)$[fm]	2.78	2.91		

Chapter 7

Conclusion

We have constructed a germanium detector system (Hyperball) for hypernuclear study and have measured γ-rays of $^7_\Lambda$Li as the first experiment. We have succeeded in observing two γ-transitions of $^7_\Lambda$Li. Those are the first observation of well-identified hypernuclear γ-rays with germanium detectors. Those two peaks were attributed to the $M1(3/2^+ \to 1/2^+)$ and $E2(5/2^+ \to 1/2^+)$ transitions, of which energies were measured to be 691.7 ± 0.6(statistical) $\pm$ 1.0(systematic) keV and 2050.4 ± 0.4(statistical) $\pm$ 0.7(systematic) keV, respectively. Precision of those energies renew the world record in hypernuclear experiments by more than one order of magnitude.

The energy of the former transition gives direct information on the strength of the ΛN spin-spin force. The present result is consistent with the spin-spin force parameter ($\Delta \sim 0.5$ MeV) estimated from the four body hypernuclear data. The strength of the ΛN spin-spin force is experimentally established.

We also have measured the lifetime of the $5/2^+$ state to be $5.8^{+0.9}_{-0.7}$(statistical)$\pm$ 0.7(systematic) ps by analyzing the peak shape of the $E2(5/2^+ \to 1/2^+)$ transition. This corresponds to a $B(E2; 5/2^+ \to 1/2^+)$ value of $3.6 \pm 0.5^{+0.5}_{-0.4}$ e^2fm^4, which gives a clear indication of the shrinkage of $^7_\Lambda$Li and thus the glue-like role of Λ is experimentally confirmed.

With those results, we have proven the usefulness of the γ-ray spectroscopy in studying hypernuclei. This experiment tells a coming of a new era of the hypernuclear physics with high-precision spectroscopy.

We are planning to continue the γ-ray spectroscopy experiments using the Hyperball. Our purpose in near future is to determine the strength of all the ΛN spin-dependent interactions. In fact, an experiment to determine the strength

of the spin-orbit interaction (V_Λ, S_Λ) using ${}^{9}_{\Lambda}$Be hypernucleus has been already carried out at BNL, and we are now analyzing the data. We are waiting for the next beamtime of BNL-AGS to complete our study.

In future, we are planning to investigate more hypernuclear physics. For example, γ-ray spectroscopy of mirror hypernuclei will enable us to study the charge symmetry breaking of the ΛN interaction. By measuring the $B(M1)$ values, we can study the effects of meson currents in hypernuclei. γ-ray spectroscopy of double-Λ hypernuclei is more challenging, but surely interesting because we can study the $\Lambda\Lambda$ interaction.

Acknowledgements

I would like to express my sincere gratitude to many people for their supports, encouragement, and advice. Particularly, I would like to thank my supervisor, Prof. Ryugo S. Hayano, who led me to the field of physics.

I am deeply indebted to Prof. Hirokazu Tamura who is the spokesperson of the Hyperball project. He taught me many things about physics and experimental techniques.

I would like to thank my collaborators, Mr. Daisuke Abe, Mr. Hisashi Akikawa, Mr. Kouta Araki, Prof. Hyoung C. Bhang, Mr. Takuya Endo, Dr. Yu Fujii, Prof. Tomokazu Fukuda, Prof. Osamu Hashimoto, Mr. Hideaki Hotchi, Prof. Kennichi Imai, Dr. Yutaka Kakiguchi, Mr. Jungho Kim, Dr. Yeongduk Kim, Mr. Toshiki Miyoshi, Dr. Tetsuya Murakami, Prof. Tomofumi Nagae, Dr. Hiroyuki Noumi, Mr. Kennichiro Ozawa, Mr. Haruhiko Outa, Prof. Teijirou Saito, Mr. Junnichi Sasao, Dr. Yoshinori Sato, Mr. Sou Satoh, Prof. Reyad I. Sawafta, Dr. Michiko Sekimoto, Dr. Toshiyuki Takahashi, Prof. Liguang Tang, Dr. Haihong Xia, Prof. Shuhua Zhou, and Dr. Lihua Zhu, for their invaluable help in the KEK-PS E419 experiment. Without them, the experiment would have never succeeded.

I would also like to thank Prof. David J. Millener, Prof. Toshio Motoba, and Dr. Emiko Hiyama for their invaluable discussions about the physics involved in the experiment. Their theoretical calculations helped us to design the experiment and to extract the physics results from the experiment. Dr. Teruhisa Morimoto had helped us in constructing the Hyperball by desinging the supporing stand. I would like to express my gratitude to him here. I would like to acknowledge the KEK staffs for their continuous support to our experiment.

Last of all, but not least, I would like to thank my colleagues in Tokyo University for their warm encouragement and simulation.

Appendix A

The (π^+, K^+) reaction

A.1 General features of the (π^+, K^+) reaction

The characteristics of the (π^+, K^+) reaction is determined mostly by the characteristics of its elementary $\pi^+ n \to K^+\Lambda$ process. This process is well known from the experimental data on the charge conjugate $\pi^- p \to K^0\Lambda$ process.

Figure A.1 shows the dependence of the cross section on the incident pion momentum for the elementary $\pi^+ n \to K^+\Lambda$ process [32]. We can see that the elementary cross section reaches maximum at $p_{\pi^+} \sim 1.05$ GeV/c. This is the reason why most of the (π^+, K^+) experiments are carried out at this incident momentum.

The (π^+, K^+) reaction is also characterized by its momentum transfer which is comparable to or larger than the nuclear fermi momentum. Figure A.2 shows the momentum transfer of the ${}^7\mathrm{Li}(\pi^+, K^+){}^7_\Lambda\mathrm{Li}$(g.s.) and the $n(\pi^+, K^+)\Lambda$ reactions. Because of this large momentum transfer, stretched hypernuclear states with large orbital angular momentum transfers are favorably populated in the (π^+, K^+) reaction.

The spin-flip and spin-nonflip amplitudes of the (π^+, K^+) reaction were obtained from the reanalysis of the experimental data on the $\pi^- p \to K^0\Lambda$ reaction by Sotona and Žofka [45]. They showed that the spin-nonflip Λ production is favored than the spin-flip production for the incident momentum of $p_{\pi^+} \sim 1.05$ GeV/c and the laboratory reaction angles of $\theta_{\mathrm{lab}} \leq 20°$, as shown in Table A.1. This feature gives a selectivity that the spin-nonflip states have larger production cross sections than spin-flip states in the hypernuclear production via the (π^+, K^+) reaction.

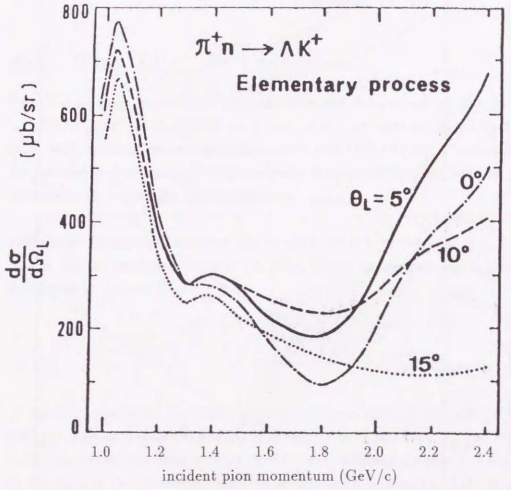

Figure A.1: *The incident pion momentum dependence of the cross section of the elementary $\pi^+ n \to K^+\Lambda$ process at several reaction angles ($\theta_{\mathrm{lab}} = 0°, 5°, 10°, 15°$) [32].*

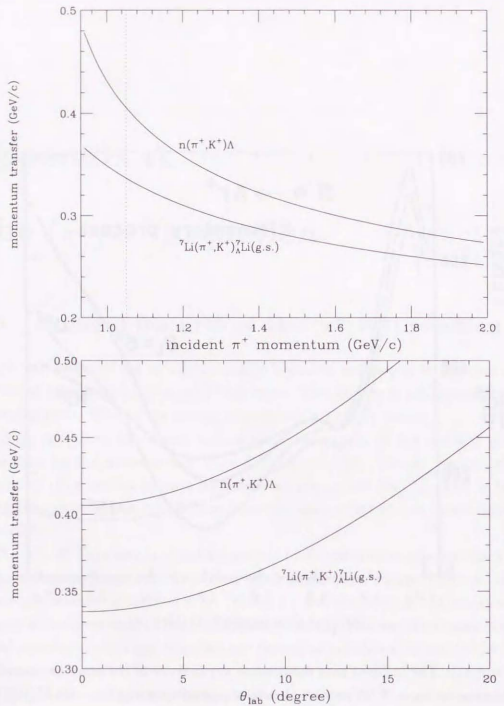

Figure A.2: *Momentum transfer of the (π^+, K^+) reactions; (Up): Momentum transfer as functions of the incident π^+ momentum at zero laboratory reaction angle. (Down): Momentum transfer as functions of the reaction angle at p_{π^+} = 1.05 GeV/c.*

Table A.1: *The elementary spin-nonflip (f) and spin-flip (g) amplitudes of the $\pi^+ n \to K^+\Lambda$ process as a function of the reaction angle ($\theta_{\rm lab}$) at p_{π^+} = 1.04 GeV/c. See Ref. [45, 32] for the definition of the f, g amplitudes.*

$\theta_{\rm lab}$	0°	5°	10°	15°	20°
$\|f\|^2$	1.056	1.022	0.928	0.793	0.641
$\|g\|^2$	0.000	0.033	0.115	0.213	0.296

A.2 The ^{7}Li(π^+, K^+) reaction

The cross sections of the ^{7}Li(π^+, K^+) reaction for the five low-lying states of $^7_\Lambda$Li $(1/2^+, 3/2^+, 5/2^+, 7/2^+, 1/2^+(T = 1)$, see Figure 1.3) are calculated by Hiyama *et al.* with distorted wave impulse approximation (DWIA) [30]. Table A.2 shows the calculated cross sections of those states integrated over $\theta_{\rm lab}$ = 0–15°, which approximately covers the SKS acceptance.

Table A.2: *Calculated cross sections of the ^{7}Li(π^+, K^+) reaction at p_{π^+} = 1.05 GeV/c for the low-lying states of $^7_\Lambda$Li [30]. Values integrated over $\theta_{\rm lab}$ = 0–15° are shown in the unit of μb.*

	$1/2^+$	$3/2^+$	$5/2^+$	$7/2^+$	$1/2^+(T=1)$
σ (μb)	1.21	0.13	1.23	0.08	0.60

As we can see from the table, the cross sections of the $3/2^+$ and $7/2^+$ states are by a order of magnitude smaller than that of their partner $(1/2^+, 5/2^+)$. This is because of the spin selectivity of the (π^+, K^+) reaction described above. Since all the spins of the valence nucleons (a proton and a neutron) and the Λ particle are parallel in those states, spin-flip Λ production is necessary to produce them from the ground state of ^{7}Li. It is noted that all those states can be produced with the same orbital angular momentum transfer, $\Delta L = 1$ and that the selection rule about orbital angular momentum transfer gives no selectivity for them.

Appendix B

Spin sequence of the doublets in ${}^{7}_{\Lambda}$Li

Throughout this thesis, we assumed the $3/2^+$ $(7/2^+)$ state is the upper part of the ground (first excited) state doublet[1]. We have been expecting this is the case because;

1. As shown in Table B.1, all the known spins of the hypernuclear ground states can be reproduced by assuming a rule that the state with smaller spin is the lower state of a doublet. This rule can be easily explained if we take the Δ parameter to be a positive value and neglect all the other parameters. Therefore, we can expect the $1/2^+$ $(5/2^+)$ state is the lower state of the ground (first excited) state doublet in ${}^{7}_{\Lambda}$Li.

   Table B.1: *The spins of the hypernuclear ground states known so far.*

	core j^π	j^π	reference
${}^{4}_{\Lambda}$H	$1/2^+({}^3\mathrm{H})$	0^+	[46]
${}^{8}_{\Lambda}$Li	$3/2^-({}^7\mathrm{Li})$	1^-	[47, 48, 49]
${}^{11}_{\Lambda}$B	$3^+({}^{10}\mathrm{B})$	$5/2^+$	[50]
${}^{12}_{\Lambda}$B	$3/2^-({}^{11}\mathrm{B})$	1^-	[51]

2. In Ref. [35], the binding energy of the $1/2^+$ state was obtained to be $-B_\Lambda = 5.6 \pm 0.1 \pm 0.2$ MeV by using the ${}^7\mathrm{Li}(\pi^+, K^+)$ reaction. On the other hand, the binding energy of the ground state of ${}^{7}_{\Lambda}$Li is known to be 5.58 ± 0.03 MeV from the experiments using emulsions [36]. Those two results give the same binding energy within the experimental errors, and thus are consistent with the present assumption. If we reverse the spin sequence keeping the absolute value of the energy difference (690 keV), the binding energy of the ground state $(3/2^+)$ becomes $6.3 \pm 0.1 \pm 0.2$ MeV from the former result. This is not consistent with the latter experimental result by more than two standard deviation.

[1]This implies the sign of the Δ parameter is positive.

Furthermore, the assumption can also be justified from the present experimental result as;

1. If we allow the case in which the $1/2^+$ $(5/2^+)$ state is located above the $3/2^+$ $(7/2^+)$ state, $M1(1/2^+ \to 3/2^+)$ and $M1(5/2^+ \to 7/2^+)$ should also be taken as candidates for the 690 keV peak. Providing the peak is assigned to the $M1(1/2^+ \to 3/2^+)$ transition, the expected yield is 361 counts from the yield of the $1/2^+$ state in Table 3.1. This is too large compared to the present experimental result. The $M1(5/2^+ \to 7/2^+)$ transition also can be ruled out by the same reason and by the discussion used to deny the possibility of the $M1(5/2^+ \to 3/2^+)$ transition in Section 5.1.

2. The yield of the 429 keV γ-ray emitted from the first excited state of ^{7}Be produced by the weak decay of ${}^{7}_{\Lambda}$Li (${}^{7}_{\Lambda}\mathrm{Li} \to {}^{7}\ \mathrm{Be}^* + \pi^-$) in the present experiment is consistent with a theoretical calculation by Motoba *et al.* [52] if we take the assumption [53]. On the other hand, if we assume the ground state is $3/2^+$, the obtained yield is one order of magnitude larger than their calculation. This gives the strongest evidence for the assumption since the elementary processes for mesonic weak decay are well known and thus uncertainties in theoretical calculations are small.

Bibliography

[1] D. J. Millener, A. Gal and C. B. Dover, Phys. Rev. C38 (1988) 2700.

[2] R.H. Dalitz and A. Gal, Ann. Phys. 116 (1978) 167; J. Phys. G 6 (1978) 889.

[3] D.J. Millener, A. Gal, C.B. Dover, R.H. Dalitz, Phys. Rev. C31 (1985) 499.

[4] V.N. Fetisov, L. Majling, J. Žofka and R.A. Eramzhyan, Z. Phys. A339 (1991) 399.

[5] D. J. Millener, private communication.

[6] M. M. Nagels, Th. A. Rijken and J. J. de Swart, Phys. Rev. D15 (1977) 2547.

[7] M. M. Nagels, Th. A. Rijken and J. J. de Swart, Phys. Rev. D15 (1979) 1633.

[8] P. M. M. Maessen, Th. A. Rijken and J. J. de Swart, Phys. Rev. C40 (1989) 2226.

[9] Th. A. Rijken, V. G. J. Stoks and Y. Yamamoto, Phys. Rev. C59 (1999) 21.

[10] B. Holzenkamp, K. Holinde and J. Speth, Nucl. Phys. A500 (1989) 485.

[11] M. Bedjidian *et al.*, Phys. Lett. 62B (1976) 467.

[12] M. Bedjidian *et al.*, Phys. Lett. 83B (1979) 252.

[13] R.E. Chrien *et al.*, Phys. Rev. C41 (1990) 1062.

[14] B. F. Gibson, I. R. Afnan, J. A. Carlson and D. R. Lehman, Prog. Theor. Phys. Suppl. 117 (1994) 339.

[15] M. May *et al.*, Phys. Rev. Lett. 51 (1983) 2085.

[16] R.H. Dalitz, Int. Sym. on Exotic Atoms and Nuclei, June 1995, Hakone, Japan (Proc. in Hyperfine Interactions, in press).

[17] T. Nagae, Proc. 23rd INS symp. on Nuclear and Particle Physics with meson beams in the 1 GeV/c region, ed. S. Sugimoto and O. Hashimoto, (Universal Academic Press, Tokyo, 1995) 175; T. Motoba, ibid 187.

[18] T. Nagae, Proc. APCTP Workshop on Strangeness Nuclear Physics (S-NP'99), ed. I. T. Cheon, S. W. Hong and T. Motoba, (World Scientific Publishing Singapore), in press.

[19] H. J. Pirner, Phys. Lett. 85B (1979) 190

[20] O. Morimatsu, S. Ohta, K. Shimizu and K. Yazaki, Nucl. Phys. A420 (1984) 573.

[21] M. Oka, Proc. Sendai International Workshop on the Spectroscopy of Hypernuclei, ed. H. Tamura, K. Maeda, T. Takahashi and O. Hashimoto (Tohoku University, Sendai, 1998) 1.

[22] S. Ajimura *et al.*, Nucl. Phys. A639 (1998) 93c.

[23] T. Fukuda *et al.*, Nucl. Inst. Meth. A 361 (1995) 485.

[24] M. May *et al.*, Phys. Rev. Lett. 78 (1997) 23.

[25] S. Cohen and D. Kurath, Nucl. Phys. 73 (1965) 1.

[26] D. J. Millener, Proc. APCTP workshop on Strangeness Nuclear Physics (SNP'99), ed. I. T. Cheon, S. W. Hong and T. Motoba, (World Scientific Publishing Singapore), in press.

[27] Y. Akaishi, Proc. APCTP workshop on Strangeness Nuclear Physics (S-NP'99), ed. I. T. Cheon, S. W. Hong and T. Motoba, (World Scientific Publishing Singapore), in press.

[28] T. Motoba, H. Bando, and H. Takaki, Z. Phys. 80 (1983) 189; T. Motoba, H. Bando, K. Ikeda and T. Yamada, Prog. Theor. Phys. Suppl. 81 (1985) 42.

[29] E. Hiyama, M. Kamimura, T. Motoba, T. Yamada and Y. Yamamoto, Phys. Rev. C. 53 (1996) 2075.

[30] E. Hiyama, M. Kamimura, K. Miyazaki and T. Motoba, Phys. Rev. C59 (1999) 2351.

[31] Table of Isotopes, 8th edition, A Wiley-Interscience Publication.

[32] H. Bandō, T. Motoba, M. Sotona and J. Žofka, Phys. Rev. C39 (1989) 587.

[33] S. Morinobu, private communication.

[34] M. Iwasaki, Low Energy Particle Simulator version 6.6, 1996 (unpublished).

[35] H. Hotchi, Master Thesis, Univ. of Tokyo(1997).

[36] R. Bertini *et al.*, Phys. Lett. 83B (1979) 306.

[37] S. Sato, Master thesis, University of Tokyo, 1998.

[38] J. F. Ziegler, The Stopping and Range of Ions in Matter, available via www at the URL: `http://www.research.ibm.com/ionbeams/home.htm#SRIM`.

[39] J. F. Ziegler, J. P. Biersack and U. Littermark, The Stopping and Range of Ions in Solids, Pergamon Press, New York, 1985.

[40] E. Hiyama, M. Kamimura, T. Motoba, T. Yamada and Y. Yamamoto, Nucl. Phys. A639 (1998) 173c.

[41] H. C. Bhang *et al.*, Nucl. Phys. A639 (1998) 269c.

[42] H. Outa *et al.*, Nucl. Phys. A547 (1992) 109c.

[43] R. Grace *et al.*, Phys. Rev. Lett. 55 (1985) 1055.

[44] J. J. Szymanski *et al.*, Phys. Rev. C43 (1991) 849.

[45] M. Sotona and J. Žofka, Prog, Theor. Phys. 81 (1989) 160; Institute for Nuclear Study, University of Tokyo Report

[46] M. M. Block *et al.*, Proc. of Int. Conf. on Hypernuclei (St. Cergue, 1964), p63.

[47] N. Crayton *et al.*, Rev. Mod. Phys. 34 (1962) 186.

[48] D. H. Davis *et al.*, Nucl. Phys. 41 (1963) 73.

[49] R. H. Dalitz, Nucl. Phys. 41 (1963) 78.

[50] D. Zieminska, Nucl. Phys. A242 (1975) 461.

[51] D. Zieminska and R. H. Dalitz, Nucl. Phys. A238 (1975) 453.

[52] T. Motoba, K. Itonaga, H. Bando, Nucl. Phys. A489 (1988) 683.

[53] J. Sasao, Master Thesis, Tohoku University, 2000; J. Sasao *et al.*, to be published.